Accepted Manuscript

Electrochemical polarization and impedance of reinforced concrete and hybrid fiber-reinforced concrete under cracked matrix conditions

Wilson Nguyen, Jacob F. Duncan, Thomas M. Devine, Claudia P. Ostertag

PII: S0013-4686(18)30651-0

DOI: 10.1016/j.electacta.2018.03.134

Reference: EA 31500

To appear in: *Electrochimica Acta*

Received Date: 12 September 2017

Revised Date: 15 March 2018

Accepted Date: 22 March 2018

Please cite this article as: W. Nguyen, J.F. Duncan, T.M. Devine, C.P. Ostertag, Electrochemical polarization and impedance of reinforced concrete and hybrid fiber-reinforced concrete under cracked matrix conditions, *Electrochimica Acta* (2018), doi: 10.1016/j.electacta.2018.03.134.

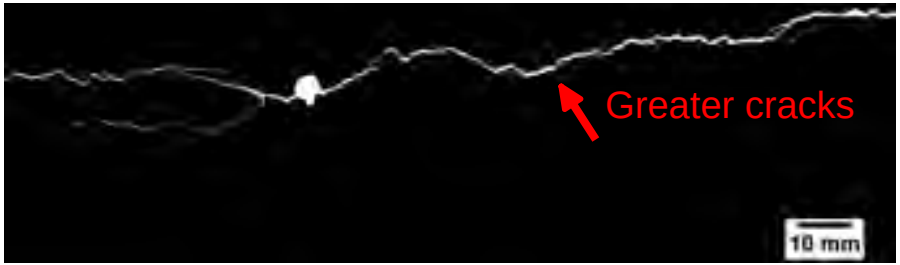

Reinforced concrete

Reinforced fiber-reinforced concrete (FRC)

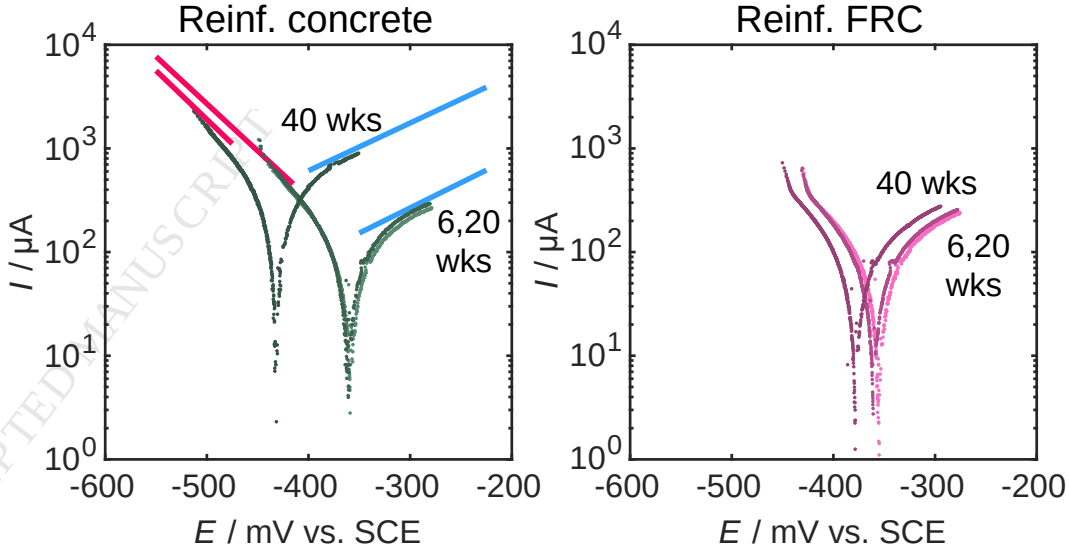

Concrete cracking changes polarization curves over time; EIS also affected by concrete cracking

Electrochemical polarization and impedance of reinforced concrete and hybrid fiber-reinforced concrete under cracked matrix conditions

Wilson Nguyen[a], Jacob F. Duncan[a], Thomas M. Devine[b] and Claudia P. Ostertag[a,*]

[a] Department of Civil & Environmental Engineering, University of California, Berkeley, CA 94720, United States
[b] Department of Materials Science & Engineering, University of California, Berkeley, CA 94720, United States
[*] Corresponding author. Tel: 510.642.0184

Emails: willnguyen@berkeley.edu (W. Nguyen), jduncan@berkeley.edu (J.F. Duncan), devine@berkeley.edu (T.M. Devine) and ostertag@ce.berkeley.edu (C.P. Ostertag)

Abstract:

In this paper, we investigate the influence of cementitious matrix cracking on the electrochemical polarization and impedance behaviors of corroding reinforced concrete and crack-resistant reinforced hybrid fiber-reinforced concrete (HyFRC). Samples were exposed to a chloride environment for 2.5 years while in either a continuous tensile stress state or in a nonloaded condition, and were periodically monitored for Tafel polarization responses. Electrochemical impedance spectroscopy (EIS) was additionally performed at the conclusion of the test program. Greater severity of corrosion-induced splitting matrix cracks along the length of embedded steel reinforcing bars and subsequent formation of anodic surfaces were found to affect several electrochemical parameters, including increase of the corrosion current and decrease of the ohmic resistance of concrete. Cathodic and anodic Tafel coefficients and Stern-Geary coefficients for passive and active samples are also reported, highlighted by a Stern-Geary coefficient of B=28.1 mV for active corrosion.

Keywords: Reinforced concrete; Corrosion; Chloride; Tafel; EIS.

1 Introduction

The electrochemical phenomenon of corrosion is a global source of deterioration of reinforced concrete structures. In environments lacking chloride ions (chlorides), low-carbon steel reinforcing bars (rebar) embedded within concrete form a passive film due to the high pH (ca. 13 to 13.5) of the concrete pore solution and are generally not expected to exhibit any significant corrosion activity during the designed service life of a structure. However, external chloride ions, which originate from sources such as ocean saltwater or deicing salts placed on roadways, can permeate porous concrete cover layers and depassivate the steel rebar after a critical threshold of local chloride concentration has been reached at the rebar surface [1, 2]. After depassivation, corrosion activity of the steel rebar readily increases. As the volume of corrosion products is greater than the sum of the reactant volumes, internal expansion of these products causes concrete cracking [3], subsequently increasing the chloride solution permeability of the concrete [4, 5] and reducing the mechanical performance of the composite [6, 7]. Premature replacement

of damaged structures and associated mass consumption of additional construction materials is undesirable due in part to the high energy demands required for concrete production [8].

Because reinforced concrete degradation is dependent on the cracked state of the composite matrix, research of novel crack-resistant construction materials has gained popularity in recent decades [9, 10]. In particular, hybrid fiber-reinforced concrete (HyFRC) is a candidate material to reduce corrosion-induced cracking damage due to the mechanical toughening provided by the inclusion of different types of short (e.g., 8-mm to 60-mm long), discontinuous fibers dispersed throughout its cementitious matrix [11, 12]. A crack-resistant concrete such as HyFRC is further advantageous considering that a primary functional purpose of reinforced concrete is to resist mechanical loads, requiring any new implemented construction material to be damage-tolerant against not only corrosion-induced cracking but also structural loading [13, 14]. An increase in the time to corrosion initiation was observed for reinforced HyFRC (i.e., HyFRC composite with embedded steel rebar) compared to reinforced concrete after subjecting samples to flexural stress [15, 16]. While a lower corrosion current density i_{corr} of reinforced HyFRC was also measured compared to reinforced concrete, indicating favorable durability performance after active corrosion had begun, electrochemical characteristics of samples were limited to corrosion potential, polarization resistance, and corrosion current density based on assumed Stern-Geary coefficients. Several corrosion-related studies with different types of fiber-reinforced concrete have utilized similar techniques [17-20], making detailed information from certain other electrochemical tests, such as Tafel polarization and electrochemical impedance spectroscopy (EIS), rarely available for fiber-reinforced concrete composites.

As mentioned, i_{corr} is an experimental parameter that is often of interest when evaluating the corrosion behavior of reinforced concrete, and may be calculated using the Stern-Geary equation if the Stern-Geary coefficient B and the polarization resistance R_p are known [21]. For reinforced concrete studies, a number of researchers have relied on the assumed values of B=52 mV and B=26 mV for passive and active steel reinforcement, respectively, referencing the paper of Andrade and González [22] published in 1978. The analysis of this paper considered a comparison between gravimetric steel mass loss and electrochemical mass loss based on time-integration of i_{corr} measurements for validation of the proposed B values. While the authors did not report values for the cathodic (β_c) or anodic (β_a) Tafel coefficients, which are typically required for determination of B (Eq. (1)), Chang et al. [23] noted that B=52 mV may be obtained by setting β_c=120 mV/decade and allowing β_a to reach infinity. Similarly, B=26 mV may be obtained by letting both Tafel coefficients be equivalent to 120 mV/decade. Though not mentioned, the assignment of β_a=120 mV/decade may be attained by evaluating the definition of the anodic Tafel slope (Eq. (2)) under standard temperature T and setting the product $\alpha_a n$=0.5, where α_a is the anodic charge transfer coefficient and n is the number of transferred electrons involved in a rate-determining step. Furthermore, R is the universal gas constant and F is the Faraday constant. A similar determination of β_c=120 mV/decade may be performed by allowing $\alpha_c n$=0.5, where α_c is the cathodic charge transfer coefficient. When assuming n=1, an electrochemical cell with α_a=0.5 and α_c=0.5 is possible, though the charge transfer coefficients should not be arbitrarily assigned to such values [24].

$$B = \frac{\beta_c \beta_a}{2.303(\beta_c + \beta_a)} \quad (1)$$

$$\beta_a = \frac{2.303RT}{\alpha_a nF} \quad (2)$$

Elsewhere in the literature, reported values of β_c, β_a, and B have generally been inconsistent, as surveyed in Table 1. Using a variety of specimen types and exposure durations, several authors have found the cathodic Tafel coefficient in actively corroding samples to be in the approximate range of 100 to 250 mV/decade [25-28], as well as in the greater range of 300 to 450 mV/decade [27, 29, 30]. Anodic Tafel coefficients of corroding steel have shown more skew, ranging from 230 mV/decade to values approaching infinity [25-27, 29, 30]. While B values for active corrosion have been determined in the range of 7 to 15 mV [31], greater values of 43 to 86 mV have also been reported [25, 27].

Cracking damage of samples, if any, were not reported in several polarization studies surveyed in Table 1 despite experimental durations reaching or exceeding 2 years [27-30]. Babaee and Castel [25] noted no corrosion-induced cracks were observed around the embedded steel rebar at the conclusion of experiments, while Grubb et al. [31] observed only microcracking in plain mortars but no cracking in fiber-reinforced mortars. Subramaniam and Bi [26] induced flexural cracking in reinforced concrete beam samples prior to chloride exposure to determine the effects of localized transverse cracking on microcell and macrocell corrosion rates, though they did not consider the effects of corrosion-induced cracking on polarization behavior.

EIS has become a common monitoring technique for reinforced concrete corrosion research in recent decades [32, 33], though few researchers have considered the influence of matrix cracking on the electrochemical impedance of corroding steel reinforcement. Feng et al. [34] subjected reinforced concrete beams to varied magnitudes of flexural stress prior to chloride exposure. The authors found that the concrete cover resistance, when modeled as an element within an equivalent electrical circuit, was not highly sensitive to the magnitude of applied flexural stress when surface concrete cracks could not be visually detected after flexural loading. However, greater applied stresses tended to decrease the circuit element value representing polarization resistance due to increased rebar-matrix interfacial damage. Similar effects of applied load-induced interfacial damage on polarization resistance [35] and charge transfer resistance [36] have been reported when using an equivalent circuit to model the electrochemical impedance spectra of reinforced concrete. While EIS can provide useful information on the effect of matrix cracking on the corrosion behavior of reinforced concrete, application of this technique on crack-resistant fiber-reinforced concrete composites remains scarcely reported in the literature. Grubb et al. [31] performed EIS on reinforced fiber-reinforced mortars subjected to chloride solution intrusion and determined that the presence of steel fibers influenced the measured impedance spectra due to the electrical conductivity of the fibers, though the authors did not provide results on equivalent circuit modeling.

Due to the aforementioned influence of cracking on the durability of reinforced concrete, a study detailing the electrochemical behavior of reinforced concrete with cracking damage is warranted to better elucidate the processes that occur while embedded steel rebar are corroding. The research presented herein investigates the long-term influence of concrete cracking on the electrochemical behavior of reinforced concrete and reinforced HyFRC in chloride environments. Prismatic samples each containing a single strand of steel reinforcing bar were subjected to external NaCl solution intrusion conditions for approximately 2.5 years, during which corrosion potential measurements, linear polarization resistance tests, and Tafel polarization tests were periodically performed to monitor changes in corrosion activity. EIS was performed at the conclusion of the environmental conditioning period to evaluate changes in the impedance responses due to accumulated matrix cracking damage. To simulate the matrix

cracking that may occur while reinforced concrete structures are in service, samples were subjected to an applied tensile load prior to, and during, exposure to the corrosion-inducing conditions.

2 Materials and methods

2.1 Materials and specimen

A hybrid fiber-reinforced concrete (HyFRC) developed by Blunt and Ostertag [12] was selected for study, and its batch proportions are presented in Table 2. The total fiber volume fraction, based on composite volume, was 1.5%. Fiber hybridization consisted of a blend of 0.04-mm diameter, 8-mm long polyvinyl alcohol (PVA) fibers; 0.55-mm diameter, 30-mm long hooked-end steel fibers; and 0.75-mm diameter, 60-mm long hooked-end steel fibers. The chemical compositions of the steel fibers, as well as of the ASTM type I/II [37] portland cement used in the mixtures, are summarized in Table 3. A combination of inductively coupled plasma, combustion, colorimetric tests, and gravimetric tests was performed on the steel fibers, while X-ray fluorescence (XRF) was performed on the cement. For the XRF testing, SO_3 could not be quantified due to its volatility during high temperature fusion. The HyFRC was evaluated against a plain concrete mixture that had the same cement content and water-cement mass ratio as HyFRC but lacked fiber reinforcement. After casting of the fresh mixtures, concrete and HyFRC specimens were cured within covered molds for 7 days, demolded, and cured an additional 21 days in ambient laboratory conditions (approximately 23.5 °C, 45% relative humidity) prior to tensile loading, if applicable. The curing regime was selected to better represent reinforced concrete construction in professional practice, where construction formwork is often removed within a few days of casting. When formwork is stripped, the concrete is exposed to ambient conditions. Compression testing of cylinders with a 100-mm diameter and 200-mm height revealed that the concrete and HyFRC had similar 28-day compressive strengths of 42.6 MPa and 44.2 MPa, respectively.

Geometric detailing of the specimen design is presented in Figure 1a. The rectangular prisms had a length of 610 mm and a square cross section with side lengths of 127 mm. A single ASTM A706 [38] steel reinforcing bar with a nominal yield stress of 410 MPa and a nominal diameter of 16 mm was placed centrally within the specimen's cross section. The alloy composition of the steel is summarized in Table 3 and was reported by a mill certificate provided upon receipt of the rebar from its commercial supplier. Prior to sample casting, the mill scale of the rebar was removed by sandblasting. The middle 406-mm length of rebar was defined to be the region of interest where corrosion was allowed to occur, and was in direct contact with the cementitious matrix during casting. Elsewhere, the reinforcing bar was coated with an electrically-insulating lacquer and then tightly wrapped with vinyl insulating tape to prevent electrical and physical contact with concrete. The extruded portions of the steel bar were threaded to allow for later tensile loading. A loading frame consisting primarily of light-gauge perforated tube steel was constructed such that specimens would remain in a stressed state while the frame would resist reactionary forces (Figure 1c).

Ponding of 3.5% w/w NaCl solution through the concrete cover was achieved by fixing a polyvinyl chloride ponding dam to a horizontal face of each of the prismatic specimens using a rubber cement adhesive, as in Figure 1b. All vertical concrete surfaces, along with the portion of the ponded specimen face not enclosed by the adhered dam, were coated with a moisture-

resisting sealant to prevent leakage of solution during experimentation. As summarized in Table 4, a total of 4 specimen types were studied, varying in composite type (concrete (C) or HyFRC) and loading state during environmental conditioning (nonloaded (0) or loaded (L)).

2.2 Tensile loading

Select specimens of each composite type were prescribed for tensile loading during chloride exposure to account for the loading of reinforced concrete that occurs in practice, which includes permanent gravity loading from the weight of supported structures as well as temporary loading such as vehicle traffic and seismic events. These loads may cause tensile concrete cracking, which is allowed under United States codes when the element is properly designed [39]. In this study, samples were loaded such that concrete cracking occurred while the steel rebar remained elastic. Based on the tensile testing results reported by Moreno et al. [40], who tested prismatic reinforced concrete and reinforced HyFRC samples with the same cross-sectional geometry and rebar size as the samples described in Figure 1, a load magnitude of 53 kN was expected to achieve the desired deformation characteristics.

The setup for loading is shown in Figure 2a while a schematic of the loading procedure is presented in Figure 2b. To load the specimens, a hydraulic pump was used to longitudinally displace one end of the steel rebar, resulting in a tensile stress and strain response along the specimen. The other, opposite end of the extruded rebar was anchored and fixed against a steel plate. After a load of 53 kN was reached, a nut located near the bearing plate where the hydraulic pump was positioned was tightened against the plate, transferring the point of force application on the rebar from the hydraulic pump to the nut. To prevent any effects of galvanic coupling between the extruded steel reinforcing bar and the steel loading frame, the frame's bearing plates were coated with an electrically-insulating spray solution and covered with vinyl insulating tape where they were to be in direct contact with the extruded rebar or bearing nut.

2.3 Environmental conditioning

To saturate the concrete after curing in ambient laboratory conditions, specimens were externally ponded with 3.5% w/w NaCl solution for 13 consecutive weeks. Afterwards, the ponding dam was completely relieved of solution for 2 weeks and then refilled with fresh solution for 2 subsequent weeks. These steps were repeated in a cyclic manner to simulate field conditions where sodium chloride solution ingress into reinforced concrete is not a continuously occurring event. After 29 total weeks of environmental conditioning, the frequency of the cycles was increased such that specimens were under drying conditions for 1 week, followed by wetting for 1 week. The total experimental corrosion monitoring time of the samples was 132 weeks, or approximately 2.5 years.

2.4 Electrochemical measurements

Corrosion activity measurements were taken periodically with a potentiostat under ambient laboratory temperature throughout the environmental conditioning period, with all measurements occurring while the specimen was in a ponded state. The potentiostat was equipped with a positive feedback iR compensation feature that corrected for the concrete cover resistance. All tests utilized a three-electrode setup, as shown in Figure 3, with the working electrode being the

steel reinforcing bar of the specimen, the counter electrode being stainless steel, and the reference electrode being a saturated calomel electrode (SCE). Stainless steel was selected as the counter electrode material based on its reported use for reinforced concrete research [41, 42]. The counter electrode and the reference electrode were immersed in a 3.5% w/w NaCl solution contained by the ponding dam. During the initial 13 weeks of environmental conditioning, measurements were taken at intervals no more than 2 weeks apart. Afterward, wet-dry cycling of samples occurred and the measurement frequency was relaxed to approximately 4-week intervals. Once 100 total weeks of environmental conditioning had elapsed, measurement sessions were further relaxed to every 6 to 10 weeks.

In a typical sample testing session, measurement of the corrosion potential E_{corr} was first performed with a duration of at least 10 minutes, during which E_{corr} was not to deviate by more than 1 mV to ensure quasi-steady state conditions. Afterwards, linear polarization resistance tests, considering a potential domain of -10 mV to 10 mV versus E_{corr}, were performed to obtain the polarization resistance R_p. The corrosion potential was again measured to ensure quasi-steady state conditions prior to conducting Tafel polarization tests, which polarized samples from a potential of 75 mV below the corrosion potential to a maximum value of 75 mV above the corrosion potential at a potential sweep rate of 0.1 mV/s. In the literature, others have utilized a magnitude of overpotential that was greater than or equivalent to 120 mV [25-27, 29, 30]. An overpotential value of 75 mV was selected for this study to minimize possible damage introduced by large applications of overpotential while being sufficiently great to allow for extraction of cathodic β_c and anodic β_a Tafel coefficients. These coefficients were determined by curve fitting of quasi-linear regions of the Tafel polarization response. After calculating the Stern-Geary coefficient B through Eq. (1), the corrosion current I_{corr} can be obtained through Eq. (3):

$$I_{corr} = \frac{B}{R_p} \tag{3}$$

Electrochemical impedance spectroscopy (EIS) was conducted at the conclusion of the environmental conditioning period. The frequency domain for testing was defined to be from 10 mHz to 100 kHz and the amplitude of the perturbation potential was 10 mV.

2.5 Destructive testing

After conclusion of the environmental conditioning phase, specimens were subjected to destructive tests to evaluate chemical, electrochemical, and physical changes caused by chloride intrusion and corrosion activity. After removing the ponding dams, cylindrical cores with a diameter of 29 mm were extracted from select samples using a coring drill press. For loaded samples, one core was taken directly over the applied load-induced macrocrack and a secondary core was taken 76 mm from the crack, as shown in Figure 4. Otherwise, a core was taken near the midlength of nonloaded samples. Coring initiated at the ponding surface and continued into the depth of the specimens, with the core drill positioned such that it would not make contact with the embedded reinforcing bar. The extracted concrete cores were cut into segments, each with a height of 25 mm, and pulverized such that the final concrete material could pass a sieve with a maximum opening of 0.84 mm.

The experimental testing standard of ASTM C1152 [43], utilizing potentiometric titration, was performed on the pulverized samples to determine their acid-soluble chloride

content, which is expected to be equivalent to the total (i.e., bound and free) amount of chlorides in the cementitious matrix. Because the test standard is specific to cement-based materials, steel fibers from HyFRC cores were manually removed after pulverizing to avoid possible artifacts introduced by oxidation of the steel fibers in acid solution. After an equivalence point of titration was determined, the chloride content was calculated as a percentage of the pulverized concrete mass used in the titration test. For HyFRC samples, this pulverized concrete mass did not include the mass of steel fibers.

Remaining specimens not subjected to coring were prepared for optical cross-sectional imaging by sawing the samples to produce a prismatic element with the steel rebar located at the approximate center of the prism, as schematically shown in Figure 5. The prismatic element was then sawed into plates approximately 13 mm thick. In the figure, hatched (i.e., shaded) portions of the extracted prism and plate indicate where the imaging surface was located. Prior to sawing, all appreciable surface cracks were impregnated with a blue-colored, low-viscosity epoxy to maintain existing crack widths and minimize any damage caused by the cutting process.

3 Results

3.1 Observed damage

Typical surface cracking of reinforced concrete and reinforced HyFRC, after application of an applied tensile load and prior to chloride exposure, is shown in Figure 6. Tensile macrocracks occurred near specimens' midlength with an approximate maximum crack width of 0.42 mm and 0.22 mm for concrete and HyFRC, respectively. For the same magnitude of applied tensile load, a smaller maximum crack width in HyFRC is expected as a result of the crack control provided by hybrid fiber reinforcement [40].

Final accumulated damage of reinforced concrete and reinforced HyFRC at the conclusion of the 132-week environmental conditioning duration is shown in Figure 7 and Figure 8, respectively. The images were obtained from an extracted prism taken from a sample of each specimen type, as previously detailed in Figure 5. Binary images (Figure 7a, Figure 7f, Figure 8a, and Figure 8f) show a vertical surface of the extracted prism. Observed macrocracks, shown in white, are contrasted with the matrix, shown in black. The middepth of the images may be slightly offset from the actual centerline of the longitudinal steel rebar embedded within the specimens. Colored lines superimposed on the binary images indicate the location of presented transverse section cuts. For instance, the transverse section cuts of sample C-0 found in Figure 7b and Figure 7c are located where the green lines occur in Figure 7a. In all transverse section images, surface voids and cracks are colored blue due to the impregnation of the samples with an epoxy containing a blue pigment. Finally, the transverse section images are positioned such that the centroid of the rebar cross section nearly coincides with the center of the presented image.

Differences in the cracking severity between concrete and HyFRC are noticeable. Matrix damage of reinforced concrete samples, regardless of applied loading state, was primarily characterized by splitting crack propagation over a considerable length of the specimens (Figure 7a and Figure 7f). Splitting cracks are identified in a longitudinal view as cracks that form along the length of a sample, and in a transverse view as cracks that emanate radially from the rebar. The presence of splitting cracks at a rebar surface generally coincided with a corroded surface (Figure 7b-e), though it is unclear which event (i.e., matrix splitting crack propagation or rebar corrosion) preceded the other for a particular transverse section. Regardless, the widespread

propagation of these cracks allowed a free path for external deleterious substances, such as NaCl solution and gaseous O_2 and CO_2, to reach the rebar surface far from the site of initial rebar corrosion and to promote depassivation or further corrosion activity.

In a nonloaded HyFRC-0 sample, transverse or splitting cracks could not be visually detected and rebar corrosion damage appeared negligible (Figure 8a-c). While under applied load, splitting cracks formed within the HyFRC-L matrix, though the crack opening and propagation length (Figure 8d-f) were significantly less severe compared to reinforced concrete samples. Splitting cracks could not propagate to the exterior of the sample due to the crack resistance of the HyFRC cover, as no surface splitting cracks were observed. Where the splitting crack widths were fine, as in Figure 8d, steel mass loss was marginal, indicating that rebar corrosion activity was generally limited to the site of the induced tensile crack near the section shown in Figure 8e.

Steel fibers embedded within chloride-contaminated HyFRC were observed to have insignificant corrosion damage, except those fibers located very near a matrix crack or located at the ponding surface itself. Similar observations of the greater chloride threshold required to corrode steel fibers as opposed to conventional steel rebar have been summarized elsewhere in the literature [10, 44].

3.2 Tafel polarization

Typical Tafel polarization curve fitting results for a passive and an active specimen are presented in Figure 9, showing the fitted cathodic and anodic polarization curves and the net current produced by the two polarization curves. The intersection of the cathodic and anodic polarization curves is where the potential $E_{I=0}$ where no net current occurs, as well as where the extracted corrosion current $I_{corr,T.}$ occurs. The subscript in $I_{corr,T.}$ indicates the result is based directly on Tafel (T.) polarization curves as shown. Generally, the most negative potentials of the raw data were ignored for fitting due to the uncharacteristically high current that occurred at these overpotentials, an experimental observation that was also noted by Chang et al. [23] Compared to active behavior, passive behavior is distinguished by greater values of potential, lower values of current, and an anodic portion of the curve exhibiting a low-angle slope as plotted. The anodic polarization curve slope is a consequence of the near potential-independence of current in the passive regime.

Cathodic and anodic Tafel coefficients β_c and β_a, respectively, are plotted in Figure 10 with $E_{I=0}$ labeled as the abscissa, while Table 5 summarizes the mean and standard deviation of β_c, β_a, and the Stern-Geary coefficient B. Two distinct clusters of data may be observed for each subplot, generally separated by corrosion potentials greater than -100 mV vs. SCE and less than -300 mV vs. SCE. The former set of measurements, totaling 71 data points, is associated with passivated samples while the latter set, totaling 156 data points, is associated with active samples. Samples not satisfying either criterion were not considered for the reported statistics.

The cathodic Tafel coefficient β_c differed between the passive regime (β_c=19.8 mV/dec) and the active regime (β_c=102 mV/dec) for steel rebar. Babaee and Castel [25] reported a similar discrepancy of β_c values between passive and active steel rebar embedded within geopolymer concrete. Changes in β_c for the same metal could be attributed to different electrochemical reduction reactions that occur at different corrosion potentials. The reduction of dissolved oxygen within basic concrete pore solution, as shown in reaction (4), is often assumed to be the reduction reaction involved in steel rebar corrosion. At lower corrosion potentials, the reduction

of hydrogen ions (i.e., H_2O), as indicated in reaction (5), could also be considered. Using the Nernst equation (Eq. (6)) at room temperature (25 °C), the equilibrium reduction potential *E* may be calculated for a given reduction reaction.

$$\frac{1}{2}O_2 + H_2O + 2e^- \rightarrow 2(OH)^- \quad (4)$$

$$2H_2O + 2e^- \rightarrow H_2 + 2(OH)^- \quad (5)$$

$$E = E^0 - \frac{0.0592}{z}\log(Q) \quad (6)$$

In Eq. (6), E^0 is the standard reduction potential, *z* is the number of electrons transferred in the cell reaction, and *Q* is the reaction quotient. For an assumed concrete pore solution pH of 13, *E* for the reduction of oxygen is determined to be 224 mV vs. SCE, which is greater than the measured corrosion potential values for any sample, as indicated in Figure 10. When considering the reduction of hydrogen ions as a possible cathodic reaction, the equilibrium reduction potential is calculated to be -1035 mV vs. SCE. Because this value is significantly lower than the lowest measured corrosion potential for any sample (i.e., lower than approximately -550 mV vs. SCE), hydrogen ions cannot be considered as a reducible species for samples with measured corrosion potentials less than -300 mV vs. SCE and its electrochemical reduction cannot contribute to an increase in β_c.

Assuming the reduction reaction for all samples is the electrochemical reduction of oxygen (reaction (4)), regardless of corrosion potential at the time of measurement, the rate-determining step (rds) at greater corrosion potentials may be the charge transfer reaction while the rds at lesser corrosion potentials may be the transport of oxygen to the electrode surface. Different rate-determining steps would result in different slopes of the cathodic polarization curve, with a greater slope (i.e., lesser β_c) expected at greater corrosion potentials when charge transfer is the rds, as observed in Table 5. However, the mean β_c value for samples at low (i.e., approximately less than -300 mV vs. SCE) measured corrosion potential was found to be 102 mV/decade, the magnitude of which being too low to suggest that diffusive transport was the rds of the reduction reaction. For comparison, a greater β_c value of 160 mV/decade was reported by Glass and Chadwick [28] to be associated with an activation-controlled oxygen reduction reaction in reinforced concrete. Additional research is proposed to elucidate the differences in measured cathodic Tafel coefficients at varied corrosion potentials.

For active samples, a mean *B*=28.1 mV was found and is similar to the well-cited value of *B*=26 mV proposed by Andrade and González [22] for reinforced concrete materials. Figure 11 plots the correlation between the corrosion current $I_{corr,S.G.}$ based on the Stern-Geary equation, which incorporates *B* directly, and the corrosion current $I_{corr,T.}$ found by extrapolation of fitted Tafel polarization responses. The dashed line in the plots is where equivalent measurements of $I_{corr,S.G.}$ and $I_{corr,T.}$ occur. For active samples, the corrosion currents from both methods of derivation are similar in magnitude and the mean values show reasonably good correlation (13.7% error). For passive samples exhibiting lower values of corrosion current, being approximately less than 10 μA based on either determination method, use of the Stern-Geary equation resulted in an underestimation of corrosion current compared to $I_{corr,T}$. When minimizing the residual between the mean values obtained from each method, an empirical Stern-Geary coefficient *B*=24.0 mV was found to be more appropriate for passivated samples.

3.3 Corrosion rate monitoring

The averaged corrosion currents I_{corr} of specimens are plotted as a function of elapsed environmental conditioning time t for the initial 12 weeks of experimentation and for the entire duration in Figure 12a and Figure 12b, respectively. The corrosion current measurements are based on Eq. (3) and directly incorporate the Stern-Geary coefficient B. For presumably passive samples, the empirical value B=24.0 mV was used for calculation. Otherwise, B was determined directly from a sample's experimental Tafel polarization response at a given time. In reinforced concrete research, the corrosion current density i_{corr} is often reported in the literature and is typically determined by normalizing I_{corr} by the nominal surface area of the rebar in contact with cementitious matrix, as the actual corroding surface area of an embedded rebar is generally not known without the use of advanced materials characterization techniques. Considering the nonuniform corrosion activity of samples in this study, as previously visualized in Figure 7 and Figure 8, communication of the corrosion current density normalized by a constant active surface area may result in inaccurate interpretations of the actual corrosion current density of samples.

Initial active corrosion of a sample was detected by an increase in I_{corr} on the order of one magnitude between consecutive measurements. Among all specimen types, loaded reinforced concrete samples (C-L) exhibited the earliest time to corrosion initiation, requiring approximately 1.0 week to become active. After 5.0 weeks, corrosion initiation was detected in loaded HyFRC-L, which was delayed compared to C-L due to the smaller crack widths produced in HyFRC upon loading. Nonloaded reinforced concrete samples (C-0) first exhibited active corrosion between 43.1 and 63.3 weeks. Compared to C-0 samples, the time to corrosion initiation for any nonloaded HyFRC sample (HyFRC-0) was at least 41.7 weeks longer and at least a factor of 1.7 longer.

The time to corrosion initiation was influenced by the diffusion rate of chlorides through the cementitious matrix. Figure 13a and Figure 13b plot the chloride content C_{Cl^-} of reinforced concrete and reinforced HyFRC, respectively, as a function of depth d from the ponding surface of the specimens. The chloride content is the mass of chlorides normalized by concrete mass in a tested sample. For HyFRC samples, steel fibers were excluded from the testing mass, as previously mentioned in Section 2.5. At the depth to the centroid of the steel reinforcing bar (d=63.5 mm), the chloride content of C-L was 0.38% wt. concrete at the cracked location and 0.32% at a noncracked location, highlighting the faster rate of chloride ingress where a crack was present and correlating with the shorter time to corrosion initiation of cracked samples as compared to noncracked samples. For HyFRC specimens not containing a macrocrack, the chloride contents were found to be in the range of 0.07 to 0.11% wt. HyFRC excluding steel fibers at the depth where the reinforcing bar was located, reduced from the chloride content found in noncracked conventional concrete at the same depth by a factor of at least 2.9. Because the concrete and HyFRC were designed with the same cement weight content and same water-cement mass ratio, differences in chloride binding from cement were likely negligible between composite types. The reduction in chloride penetration could then be attributed to the presence of fiber reinforcement in sound matrices. The inclusion of PVA or steel fibers has been experimentally observed to retard the rate of chloride ingress in cementitious composites [45-47]. In the absence of macrocracks, use of hybrid fiber reinforcement may be used as an effective corrosion initiation retardant for its decrease in effective chloride permeation rate, though the precise influence of fibers on chloride diffusion requires further investigation.

3.4 Electrochemical impedance spectroscopy

Selection of an appropriate equivalent electrical circuit that models the potentiostatic EIS results of a metal considers three parallel paths: (1) the impedance associated with the oxidation reaction; (2) the impedance associated with the reduction reaction; and (3) the impedance associated with the capacitance of the electrode-electrolyte solution interface. The oxidation reactions result in pitting corrosion and passive film growth. While reduction reactions can take place within a pit, only the reduction of oxygen on the steel surface outside a pit is considered herein. The impedance related to pitting corrosion was reported by Wenger et al. [48] to short-circuit the impedance associated with passive film growth and reduction of oxygen.

A circuit containing two time constants, as shown in Figure 14a, was suitable for modeling the behavior of conventional reinforced concrete and is similar to the equivalent circuit described by others of steel reinforcing bars undergoing corrosion within reinforced concrete [49-51]. Constant-phase elements (CPE) were used in the equivalent circuit to account for the nonideal behavior of capacitor elements. The impedance Z_{CPE} of a CPE is described by Eq. (7):

$$Z_{CPE} = \frac{1}{Y_0(j\omega)^{\alpha}} \qquad (7)$$

Y_0 is the admittance modulus of an ideal capacitor, j is the imaginary unit, ω is the angular frequency, and α is an exponent ranging from 0 to 1. A value of 1 for α describes an ideal capacitor, a value of 0.5 describes an infinite Warburg diffusion-controlled element, and a value of 0 describes a resistor. At the base of corrosion pits, the element designated as CPE_{DL} represents the double-layer capacitance while the element R_{CT} accounts for the charge transfer resistance of the oxidation reaction. These two parallel elements are connected in series to the resistor R_{pit}, which accounts for the resistance related to ion transport through the electrolyte solution in corrosion pits. The remaining constant phase element, CPE_{pass}, relates to the capacitance of the double-layer at the interface between the passive film and concrete pore solution and the capacitance of the passive film. Capacitances related to CPE_{pass} occur in series, with the double-layer capacitance likely greater than that of the passive film, resulting in the total capacitance CPE_{pass} approximated as the double-layer capacitance. Finally, the ohmic resistance of the concrete solution is represented by the element R_{soln} and is attributed to solution-filled pores and cracks in the matrix.

After unsatisfactory fitting of data from HyFRC samples to the described equivalent circuit, a constant phase element (CPE_{fiber}) was placed parallel to R_{soln}, as shown in Figure 14b, to account for steel fiber-matrix interfaces that occur for an arrangement of continuously connected fibers. Within the cementitious matrix, fibers are in contact with each other due to their nonuniform spatial distribution resulting from concrete mixing and casting [52]. Any resistance from the concrete pore solution between the imperfect contact of steel fibers was assumed to be negligible relative to R_{soln}, which considers a relatively large concrete cover (56 mm) compared to the small distances between nearly contacting steel fibers in the matrix.

Bode plots comparing the fitting results of the impedance modulus $|Z|$ and negative phase shift $-\Phi$ to acquired EIS data are presented in Figure 15a and Figure 15b, respectively. EIS measurements were taken at the conclusion of the environmental conditioning period, and thus consider the influence of matrix cracking, if any. Good correlation is observed between the experimental data and the model fit. At intermediate to high testing frequencies f (i.e., f greater than approximately 1 Hz to 10 Hz), the impedance modulus of reinforced HyFRC samples

decreases more rapidly with increasing frequency compared to that of reinforced concrete samples. Grubb et al. [31] observed a similar deviation between the impedance modulus spectra of steel rebar embedded within steel fiber-reinforced mortar and plain mortar. Nyquist plots relating the negative imaginary part $-Z_{im}$ of the complex impedance to the real part Z_{re} of the complex impedance are presented in Figure 15c and Figure 15d at different plot scales. In these plots, a lower value of Z_{re} is associated with a greater testing frequency. While the responses of C-0 and C-L, as shown in Figure 15c, are characterized by a single minimum, the HyFRC-L response contains two minima, with one of the minima located at low values of Z_{re}, or conversely, high tested frequency f. This minimum at high tested frequency is characteristic of steel fiber inclusion in the HyFRC matrix, and is also present in the response of HyFRC-0. Similar effects of steel fibers on Nyquist plot responses of concrete materials have been reported by others [53-55], though these authors did not consider the impedance spectra with a steel rebar embedded within concrete. Passivity of the rebar within the HyFRC-0 sample dominated its impedance response, resulting in a considerably different response compared to HyFRC-L at lower tested frequencies, as exhibited in Figure 15d.

Values of the parameters used in the equivalent circuit modeling, in addition to corrosion current, are summarized in Table 6 for considered specimens. The corrosion currents were determined in the same manner as described in Section 3.3. Similar to the reporting of corrosion current rather than corrosion current density, the EIS parameter values are not scaled by the area affected by pitting corrosion due to this area not being accurately known during electrochemical testing. The ohmic concrete resistance R_{soln}, determined to be 3.07 to 6.93 Ω for reinforced concrete, was greater for HyFRC-L (28.8 Ω) and was one order of magnitude greater for HyFRC-0. Due to the presence of longitudinal splitting cracks that reached the specimen surface in both reinforced concrete specimens, a direct path with greater void volume saturated by solution was available from the steel rebar to the surface of the concrete. Cracks within the HyFRC-L matrix were finer compared to those in reinforced concrete, resulting in a greater electrolyte solution resistance for the HyFRC sample. Lower charge transfer resistances R_{CT} were noted for samples with greater I_{corr}. While R_{CT} of loaded samples were similar in magnitude to the nonloaded reinforced concrete sample C-0, the charge transfer resistance of HyFRC-0 was four orders of magnitude greater than the other considered specimens due to the oxidation of this specific specimen attributed almost entirely to passive film growth and to marginal amounts of pitting corrosion. As previously visualized in Figure 7 and Figure 8, noticeable pitting corrosion was found for the HyFRC-L, C-0, and C-L sample types, with greater corrosion damage observed for greater matrix cracking severity. Similarly, the R_{pit} value for HyFRC-0 was greater than that of other considered samples.

Circuit element values for the constant phase elements CPE_{DL} and CPE_{pass} differed between sample types. For reinforced concrete and reinforced HyFRC samples, the exponent term α for CPE_{DL} was determined to be 0.297 to 0.336 and 0.632 to 0.807, respectively. The values of α were low (i.e., on the order of 0.3) for the reinforced concrete samples. Similarly low values were reported by Dhouibi-Hachani et al. [56] for reinforced concrete samples immersed in solutions containing chloride, sulfate, or both. The authors found that the value of α correlated with the nonuniform arrangement of corrosion pits as well as the heterogeneity of corrosion products on the steel bar surface and in the concrete pores adjacent to the steel bar surface, with lower α associated with greater levels of inhomogeneity. Similar remarks concerning the relationship between α and surface heterogeneity have been reported in the literature [57, 58].

Lower α values were noted for reinforced concrete samples compared to those of reinforced HyFRC due to more extensive pitting corrosion on the steel rebar surface.

The α values for CPE_{pass} in reinforced HyFRC were determined to be 0.502 to 0.512. As α=0.5 describes an infinite Warburg element, it is suggested that CPE_{pass} is a diffusion-controlled element for the HyFRC samples. The passive film of steel in simulated concrete pore solution was modeled by Sánchez et al. [59] as a Warburg element representing the diffusion of oxygen vacancies through the passive film. Compared to noncracked conventional concrete sections, noncracked HyFRC sections were found to exhibit a relatively low chloride content in the matrix pore solution at the depth of the reinforcing bar, as previously detailed in Figure 13. It is likely that the HyFRC generally maintained an insignificantly damaged passive film at cathodic surfaces, while the higher chloride content in the pore solution of conventional reinforced concrete caused damage to the film, resulting in lower α values (0.306 to 0.325).

Fitting of CPE_{fiber}, which accounted for the impedance contribution of embedded steel fibers in the HyFRC matrix, was determined to have an exponent term α in the range of 0.493 to 0.508. The steel fibers in the matrix are also best described as a Warburg diffusion element due to α being nearly equivalent to the value of 0.5, suggesting that the bulk of fibers should be in a passivated state. As previously mentioned in Section 3.1, steel fibers embedded within sound HyFRC did not appear to exhibit corrosion damage, indicating the fitting results coincided with visual observations.

4 Discussion

4.1 Early-age corrosion propagation

Changes in the Tafel polarization responses of select samples during the initial 40 weeks of active corrosion are presented in Figure 16. The indicated time in the plots is the elapsed active corrosion time, which is considered to be 0 weeks upon first detection of corrosion initiation. HyFRC-0 did not produce sufficient active corrosion measurements during the experiment to consider for appropriate comparison.

The early-age corrosion propagation characteristics were influenced by composite type and presence of matrix cracks. For the nonloaded sample C-0, insignificant changes are observed for the polarization curves at 6 and 20 weeks. Later, a shift in the polarization response at 40 weeks is characterized by a large current increase in the anodic reaction curve, as highlighted by the arrow in Figure 16a. By comparison, the cathodic reaction curve is only slightly shifted to lesser values of potential. An increase in anodic current may be caused by an increase in chloride concentration of the local solution at the rebar surface [60-63], an increase in the actively corroding surface area, or both. Cracking of the concrete matrix would allow both events to occur, as splitting cracks with sufficient width increase the chloride solution permeability of the concrete cover [4, 5] and subsequently cause passivated surfaces within the splitting crack wake to become active. The large shift of the anodic curve results in an increase in corrosion current from 20 to 40 weeks, as highlighted in Figure 16d. While loaded specimen C-L exhibits a greater corrosion current at 6 weeks compared to C-0, the polarization response of C-L does not significantly change from 6 to 40 weeks. Because corrosion products preferentially form within defects (i.e., cracks) located near the steel rebar surface [64, 65], the corrosion rate of C-L is initially higher due to products more readily forming within empty crack openings than in a denser rebar-matrix interface. Corrosion-induced matrix cracking occurs when the accumulation

of expansive corrosion products fills a void volume and places sufficient stresses on the matrix, an event which likely did not occur until after 40 weeks of active corrosion. Due to a lack of additional matrix cracking, the corrosion rate does not increase as rapidly compared to that of C-0 despite being initially greater.

Although HyFRC-L was also exposed to a chloride environment while in a cracked and loaded condition, its corrosion current was lower compared to C-L due to the fineness of the cracks in the HyFRC matrix, resulting in a smaller initial anodic surface where the crack-rebar interface was located. A decrease in HyFRC-L corrosion potential occurs at 40 weeks and the corrosion rate (107 μA) is slightly reduced from the measurement obtained at 20 weeks (113 μA) despite an increase in the anodic reaction curve to greater current. Lowering of the corrosion rate is caused in part by shifting of the equilibrium potential *E* of the cathodic reaction to a more negative value of potential. Based on the Nernst equation and the oxygen reduction reaction previously presented in (4), a change in the equilibrium potential of the cathodic reaction may be anticipated based on changes in solution chemistry as described by Eq. (8):

$$E = E^0 - \frac{0.0592}{z}\log\left(\frac{[(OH)^-]^2}{p_{O_2}1/2}\right) \qquad (8)$$

E^0 is the standard reduction potential, z is the number of electrons transferred in the cell reaction, $[(OH)^-]$ is the concentration of OH^- in solution, and p_{O_2} is the partial pressure of dissolved O_2 in solution. The equilibrium potential lowers for increasing concentration of hydroxide or decreasing partial pressure of dissolved oxygen. The former change in chemistry is unlikely due to the inherently high pH of concrete pore solution (ca. 13 to 13.5) and a tendency for pH to decrease due to carbonation or calcium hydroxide leaching of the cementitious matrix. A lowering of oxygen partial pressure is more likely and may be caused by several phenomena, including the formation of corrosion product scales on the steel rebar surface, which impede the diffusion of oxygen through the scale layers [66, 67], and a greater consumption of oxygen in electrode reactions than replenishment [68, 69], which leaves the oxygen partial pressure lowered at the time of measurement. Samples remained under activation-controlled kinetics, as previously mentioned in Section 3.2. While both C-0 and HyFRC-L exhibit a shifting of cathodic reaction curves from 20 to 40 weeks, the increase in anodic current is significantly greater for C-0 due to the poorer crack resistance of the plain matrix compared to that of the fiber-reinforced matrix of HyFRC.

4.2 Late-age corrosion propagation

Tafel polarization diagrams showing responses for up to 90 weeks of corrosion activity for C-0 and up to 130 weeks of corrosion activity for C-L and HyFRC-L are presented in Figure 17. C-0 is characterized by the greatest increases in corrosion current as corrosion propagation time increases, followed by C-L and then HyFRC-L. Greater corrosion current was correlated with greater splitting crack damage, which was previously mentioned to increase the permeability of the cementitious matrix and allow for the ingress of chlorides and oxygen to the steel rebar surface through cracks. For C-0 and C-L, the maximum surface splitting crack widths were measured to be 0.32 mm and 0.14 mm, respectively. While HyFRC-L exhibited local splitting crack damage near actively corroding rebar surfaces, as previously shown in Figure 8, no surface splitting cracks could be visually detected on the exterior surface of any HyFRC sample.

Correspondingly, the corrosion rate of HyFRC-L shows small increases from 40 to 70 weeks though does not significantly change after 70 weeks.

Evaluation of the fitted cathodic and anodic reaction curves from polarization responses taken at 90 weeks of active corrosion, as shown in Figure 18, highlight the dominating effect of the anodic response on $I_{corr,T.}$ compared to the cathodic response. Due in majority to the increased anodic current, the corrosion currents of C-0 and C-L are greater than the corrosion current of HyFRC-L, designated as $I_{corr,T.(HyFRC-L)}$, by factors of 5.78 and 2.21, respectively. Use of hybrid fiber reinforcement may be regarded as a method to reduce the total corrosion current of reinforced concrete over long-term conditions due to its effective crack control, which restricts pitting corrosion of large surfaces of the steel rebar far from the initial site of corrosion.

5 Summary and conclusions

The corrosion behavior of conventional reinforced concrete and reinforced hybrid fiber-reinforced concrete (HyFRC) was found to be highly dependent on the cracked state of the composite matrix. A corrosive environment was prepared by allowing 3.5% w/w NaCl solution to permeate the porous cementitious matrix of samples containing a single steel reinforcing bar (rebar) in a wet-dry cyclic manner over a 2.5-year experimental duration. To account for cracks that are present in civil engineering structures in service, subsets of specimens were subjected to the same applied tensile load during environmental exposure. Corrosion potential measurements, linear polarization tests, and Tafel polarization tests were periodically conducted to monitor the electrochemical response of samples during the experiment. In addition, electrochemical impedance spectroscopy (EIS) was performed to evaluate the differences in the impedance responses between samples as a result of accumulated matrix cracking. The following conclusions are made:

1. HyFRC composites require a longer time to initiate steel rebar corrosion compared to conventional reinforced concrete. While placed under tensile stress and subsequently cracked, the delay is attributed to the crack control of fiber reinforcement restricting the maximum opening of induced cracks, which slows the rate of external NaCl solution penetration. For nonloaded samples, the inclusion of polyvinyl alcohol (PVA) and steel fibers reduces the effective chloride ion diffusion rate through the matrix and lengthens the time to achieve active corrosion by a factor of at least 1.7, though the detailed mechanism of retardation requires additional study.
2. The cathodic and anodic Tafel coefficients for actively corroding samples, regardless of composite or loading condition, were found to have mean values of β_c=102 mV/decade and β_a=180 mV/decade, respectively. A mean Stern-Geary coefficient of B=28.1 mV was also calculated, similar to the well-cited value of B=26 mV for active corrosion of reinforced concrete proposed by Andrade and González [22]. For passive samples, use of B based on fitted Tafel coefficients resulted in an underestimation of the corrosion current compared to the corrosion current extrapolated directly from Tafel polarization curves. In this case, an adjusted Stern-Geary coefficient of B=24.0 mV was used for passive samples based on empirical fitting.
3. At the conclusion of testing, matrix cracking damage was most severe for nonloaded reinforced concrete (C-0). In order of descending observed damage, loaded reinforced concrete (C-L), loaded reinforced HyFRC (HyFRC-L), and finally nonloaded reinforced

HyFRC (HyFRC-0) followed. Upon initial active corrosion, stress accumulation and subsequent cracking from expansive corrosion product formation occur more rapidly for C-0 due to the formation of such products in a dense rebar-matrix interface rather than within a crack void. HyFRC was significantly more effective than conventional concrete at restricting the opening and propagation of corrosion-induced cracks.

4. Correlating with the most severe cracking damage among sample types, C-0 was associated with the lowest charge transfer resistance and lowest ohmic concrete pore solution resistance, as well as the highest corrosion current. Correspondingly, the charge transfer and pore solution resistances were greater and the corrosion current was lower for HyFRC-L compared to reinforced concrete samples due to less severe matrix cracking.
5. The exponent term α for constant phase elements of equivalent circuits for EIS modeling had lower magnitude of value for greater pitting corrosion severity. Considering the constant phase element representing the interfacial capacitance and passive film of steel rebar (CPE_{pass}), α was determined to be approximately 0.5 for HyFRC samples, indicating that the element acted as a diffusion-controlled infinite Warburg element that was not significantly damaged. The result correlates well with low measured chloride ion contents in the matrix of noncracked HyFRC sections.
6. While the analysis of Tafel polarization curves indicate that the partial pressure of reducible oxygen in the concrete pore solution decreased over time, which would otherwise lower the corrosion rate if no other changes occurred, increasing corrosion currents occurred for reinforced concrete samples during the testing duration while active HyFRC did not significantly change in corrosion rate for the final 40 weeks of experimentation. Increases in corrosion current were primarily attributed to the formation of additional active steel rebar surfaces beyond the initial site of corrosion, which was made possible by the formation of matrix splitting cracks along the length of the rebar and was more widespread for reinforced concrete. Control of the anodic current response is regarded as being critical for preventing increasing corrosion rates in reinforced concrete composites undergoing wet-dry cycling.

Acknowledgments

This work was supported by the Federal Highway Administration (FHWA) of the United States Department of Transportation [grant DTFH61-09-R-00017]. W. Nguyen was additionally supported by the Carlson-Polivka Fellowship. The authors would like to thank Gabriel Jen for discussions related to the content of this paper, as well as Tamika Bassman and Matthew Landberg for their exceptional contributions as undergraduate student researchers.

References

[1] V.K. Gouda, Corrosion and corrosion inhibition of reinforcing steel: I. Immersed in alkaline solutions, Br Corros J, 5 (1970) 198-203.
[2] D.A. Hausmann, Steel corrosion in concrete-How does it occur?, Mater Prot, 6 (1967) 19-23.
[3] C. Andrade, C. Alonso, F.J. Molina, Cover cracking as a function of bar corrosion: Part I-Experimental test, Mater Struct, 26 (1993) 453-464.
[4] Y. Li, X. Chen, L. Jin, R. Zhang, Experimental and numerical study on chloride transmission in cracked concrete, Constr Build Mater, 127 (2016) 425-435.

[5] H. Ye, N. Jin, X. Jin, C. Fu, Model of chloride penetration into cracked concrete subject to drying–wetting cycles, Constr Build Mater, 36 (2012) 259-269.
[6] K. Andisheh, A. Scott, A. Palermo, Seismic behavior of corroded RC bridges: Review and research gaps, Int J Corros, 2016 (2016) 1-22.
[7] Y. Zhou, B. Gencturk, K. Willam, A. Attar, Carbonation-induced and chloride-induced corrosion in reinforced concrete structures, J Mater Civ Eng, 27 (2015) 04014245.
[8] P.J.M. Monteiro, S.A. Miller, A. Horvath, Towards sustainable concrete, Nat Mater, 16 (2017) 698-699.
[9] Y. Li, X. Liu, J. Li, Experimental study of retrofitted cracked concrete with FRP and nanomodified epoxy resin, J Mater Civ Eng, 29 (2017) 04016275.
[10] C.G. Berrocal, K. Lundgren, I. Löfgren, Corrosion of steel bars embedded in fibre reinforced concrete under chloride attack: State of the art, Cem Concr Res, 80 (2016) 69-85.
[11] G. Jen, W. Trono, C.P. Ostertag, Self-consolidating hybrid fiber reinforced concrete: Development, properties and composite behavior, Constr Build Mater, 104 (2016) 63-71.
[12] J. Blunt, C.P. Ostertag, Deflection hardening and workability of hybrid fiber composites, ACI Mater J, 106 (2009) 265-272.
[13] W. Nguyen, W. Trono, M. Panagiotou, C.P. Ostertag, Seismic response of a rocking bridge column using a precast hybrid fiber-reinforced concrete (HyFRC) tube, Compos Struct, 174 (2017) 252-262.
[14] M.J. Bandelt, S.L. Billington, Bond behavior of steel reinforcement in high-performance fiber-reinforced cementitious composite flexural members, Mater Struct, 49 (2014) 71-86.
[15] G. Jen, C.P. Ostertag, Experimental observations of self-consolidated hybrid fiber reinforced concrete (SC-HyFRC) on corrosion damage reduction, Constr Build Mater, 105 (2016) 262-268.
[16] J. Blunt, G. Jen, C.P. Ostertag, Enhancing corrosion resistance of reinforced concrete structures with hybrid fiber reinforced concrete, Corros Sci, 92 (2015) 182-191.
[17] C.G. Berrocal, I. Löfgren, K. Lundgren, L. Tang, Corrosion initiation in cracked fibre reinforced concrete: Influence of crack width, fibre type and loading conditions, Corros Sci, 98 (2015) 128-139.
[18] S.C. Paul, G.P.A.G. van Zijl, Crack formation and chloride induced corrosion in reinforced strain hardening cement-based composite (R/SHCC), J Adv Concr Technol, 12 (2014) 340-351.
[19] A. Michel, A.O.S. Solgaard, B.J. Pease, M.R. Geiker, H. Stang, J.F. Olesen, Experimental investigation of the relation between damage at the concrete-steel interface and initiation of reinforcement corrosion in plain and fibre reinforced concrete, Corros Sci, 77 (2013) 308-321.
[20] S. Miyazato, Y. Hiraishi, Durability against steel corrosion of HPFRCC with bending cracks, J Adv Concr Technol, 11 (2013) 135-143.
[21] M. Stern, A.L. Geary, Electrochemical polarization I. A theoretical analysis of the shape of polarization curves, J Electrochem Soc, 104 (1957) 56-63.
[22] C. Andrade, J.A. González, Quantitative measurements of corrosion rate of reinforcing steels embedded in concrete using polarization resistance measurements, Mater Corros, 29 (1978) 515-519.
[23] Z.-T. Chang, B. Cherry, M. Marosszeky, Polarisation behaviour of steel bar samples in concrete in seawater. Part 1: Experimental measurement of polarisation curves of steel in concrete, Corros Sci, 50 (2008) 357-364.

[24] R. Guidelli, R.G. Compton, J.M. Feliu, E. Gileadi, J. Lipkowski, W. Schmickler, S. Trasatti, Defining the transfer coefficient in electrochemistry: An assessment (IUPAC Technical Report), Pure Appl Chem, 86 (2014) 245-258.
[25] M. Babaee, A. Castel, Chloride-induced corrosion of reinforcement in low-calcium fly ash-based geopolymer concrete, Cem Concr Res, 88 (2016) 96-107.
[26] K.V. Subramaniam, M. Bi, Investigation of steel corrosion in cracked concrete: Evaluation of macrocell and microcell rates using Tafel polarization response, Corros Sci, 52 (2010) 2725-2735.
[27] Z.-T. Chang, B. Cherry, M. Marosszeky, Polarisation behaviour of steel bar samples in concrete in seawater. Part 2: A polarisation model for corrosion evaluation of steel in concrete, Corros Sci, 50 (2008) 3078-3086.
[28] G.K. Glass, J.R. Chadwick, An investigation into the mechanisms of protection afforded by a cathodic current and the implications for advances in the field of cathodic protection, Corros Sci, 36 (1994) 2193-2209.
[29] C. Alonso, C. Andrade, M. Izquierdo, X.R. Nóvoa, M.C. Pérez, Effect of protective oxide scales in the macrogalvanic behaviour of concrete reinforcements, Corros Sci, 40 (1998) 1379-1389.
[30] A.-H.J. Al-Tayyib, M.S. Khan, Corrosion rate measurements of reinforcing steel in concrete by electrochemical techniques, ACI Mater J, 85 (1988) 172-177.
[31] J.A. Grubb, J. Blunt, C.P. Ostertag, T.M. Devine, Effect of steel microfibers on corrosion of steel reinforcing bars, Cem Concr Res, 37 (2007) 1115-1126.
[32] X.R. Nóvoa, Electrochemical aspects of the steel-concrete system. A review, J Solid State Electrochem, 20 (2016) 2113-2125.
[33] H.-W. Song, V. Saraswathy, Corrosion monitoring of reinforced concrete structures - A review, Int J Electrochem Sci, 2 (2007) 1-28.
[34] X. Feng, X. Lu, Y. Zuo, N. Zhuang, D. Chen, Electrochemical study the corrosion behaviour of carbon steel in mortars under compressive and tensile stresses, Corros Sci, 103 (2016) 66-74.
[35] X.-H. Wang, B. Chen, Y. Gao, J. Wang, L. Gao, Influence of external loading and loading type on corrosion behavior of RC beams with epoxy-coated reinforcements, Constr Build Mater, 93 (2015) 746-765.
[36] A. Ababneh, M. Sheban, Impact of mechanical loading on the corrosion of steel reinforcement in concrete structures, Mater Struct, 44 (2010) 1123-1137.
[37] ASTM International, ASTM C150/C150M-12, Standard specification for portland cement, ASTM International, West Conshohocken, PA, 2012.
[38] ASTM International, ASTM A706/A706M-13, Standard specification for low-alloy steel deformed and plain bars for concrete reinforcement, ASTM International, West Conshohocken, PA, 2013.
[39] ACI Committee 318, Building code requirements for structural concrete (ACI 318-11), American Concrete Institute, Farmington Hills, Mi, 2011.
[40] D.M. Moreno, W. Trono, G. Jen, C. Ostertag, S.L. Billington, Tension stiffening in reinforced high performance fiber reinforced cement-based composites, Cem Concr Compos, 50 (2014) 36-46.
[41] I. Martínez, C. Andrade, Polarization resistance measurements of bars embedded in concrete with different chloride concentrations: EIS and DC comparison, Mater Corros, 62 (2011) 932-942.

[42] C. Andrade, C. Alonso, Test methods for on-site corrosion rate measurement of steel reinforcement in concrete by means of the polarization resistance method, Mater Struct, 37 (2004) 623-643.
[43] ASTM International, ASTM C1152/C1152M-04, Standard test method for acid-soluble chloride in mortar and concrete, ASTM International, West Conshohocken, PA, 2004.
[44] V. Marcos-Meson, A. Michel, A. Solgaard, G. Fischer, C. Edvardsen, T.L. Skovhus, Corrosion resistance of steel fibre reinforced concrete - A literature review, Cem Concr Res, 103 (2018) 1-20.
[45] C. Frazão, A. Camões, J. Barros, D. Gonçalves, Durability of steel fiber reinforced self-compacting concrete, Constr Build Mater, 80 (2015) 155-166.
[46] B. Kim, A.J. Boyd, H.S. Kim, S.H. Lee, Steel and synthetic types of fibre reinforced concrete exposed to chemical erosion, Constr Build Mater, 93 (2015) 720-728.
[47] S. Abbas, A.M. Soliman, M.L. Nehdi, Chloride ion penetration in reinforced concrete and steel fiber-reinforced concrete precast tunnel lining segments, ACI Mater J, 111 (2014) 613-622.
[48] F. Wenger, S. Cheriet, B. Talhi, J. Galland, Electrochemical impedance of pits. Influence of the pit morphology, Corros Sci, 39 (1997) 1239-1252.
[49] J. Wei, X.X. Fu, J.H. Dong, W. Ke, Corrosion evolution of reinforcing steel in concrete under dry/wet cyclic conditions contaminated with chloride, J Mater Sci Technol, 28 (2012) 905-912.
[50] A. Królikowski, J. Kuziak, Impedance study on calcium nitrite as a penetrating corrosion inhibitor for steel in concrete, Electrochim Acta, 56 (2011) 7845-7853.
[51] G. Qiao, J. Ou, Corrosion monitoring of reinforcing steel in cement mortar by EIS and ENA, Electrochim Acta, 52 (2007) 8008-8019.
[52] J.-P. Suuronen, A. Kallonen, M. Eik, J. Puttonen, R. Serimaa, H. Herrmann, Analysis of short fibres orientation in steel fibre-reinforced concrete (SFRC) by X-ray tomography, J Mater Sci, 48 (2012) 1358-1367.
[53] B. Suryanto, W.J. McCarter, G. Starrs, G.V. Ludford-Jones, Electrochemical immittance spectroscopy applied to a hybrid PVA/steel fiber engineered cementitious composite, Mater Des, 105 (2016) 179-189.
[54] T.O. Mason, M.A. Campo, A.D. Hixson, L.Y. Woo, Impedance spectroscopy of fiber-reinforced cement composites, Cem Concr Compos, 24 (2002) 457-465.
[55] J.M. Torrents, T.O. Mason, A. Peled, S.P. Shah, E.J. Garboczi, Analysis of the impedance spectra of short conductive fiber-reinforced composites, J Mater Sci, 36 (2001) 4003-4012.
[56] L. Dhouibi-Hachani, E. Triki, J. Grandet, A. Raharinaivo, Comparing the steel-concrete interface state and its electrochemical impedance, Cem Concr Res, 26 (1996) 253-266.
[57] Z. Yao, Z. Jiang, F. Wang, Study on corrosion resistance and roughness of micro-plasma oxidation ceramic coatings on Ti alloy by EIS technique, Electrochim Acta, 52 (2007) 4539-4546.
[58] U. Rammelt, G. Reinhard, On the applicability of a constant phase element (CPE) to the estimation of roughness of solid metal electrodes, Electrochim Acta, 35 (1990) 1045-1049.
[59] M. Sánchez, J. Gregori, C. Alonso, J.J. García-Jareño, H. Takenouti, F. Vicente, Electrochemical impedance spectroscopy for studying passive layers on steel rebars immersed in alkaline solutions simulating concrete pores, Electrochim Acta, 52 (2007) 7634-7641.
[60] G. Liu, Y. Zhang, Z. Ni, R. Huang, Corrosion behavior of steel submitted to chloride and sulphate ions in simulated concrete pore solution, Constr Build Mater, 115 (2016) 1-5.

[61] C.-Q. Ye, R.-G. Hu, S.-G. Dong, X.-J. Zhang, R.-Q. Hou, R.-G. Du, C.-J. Lin, J.-S. Pan, EIS analysis on chloride-induced corrosion behavior of reinforcement steel in simulated carbonated concrete pore solutions, J Electroanal Chem, 688 (2013) 275-281.
[62] L. Jiang, G. Huang, J. Xu, Y. Zhu, L. Mo, Influence of chloride salt type on threshold level of reinforcement corrosion in simulated concrete pore solutions, Constr Build Mater, 30 (2012) 516-521.
[63] T. Liu, R.W. Weyers, Modeling the dynamic corrosion process in chloride contaminated concrete structures, Cem Concr Res, 28 (1998) 365-379.
[64] B. Šavija, M. Luković, S.A.S. Hosseini, J. Pacheco, E. Schlangen, Corrosion induced cover cracking studied by X-ray computed tomography, nanoindentation, and energy dispersive X-ray spectrometry (EDS), Mater Struct, 48 (2014) 2043-2062.
[65] R. Zhang, A. Castel, R. François, Concrete cracking due to chloride-induced reinforcement corrosion – influence of steel–concrete interface defects due to the 'top-bar effect', Eur J Environ Civ Eng, 16 (2012) 402-413.
[66] Y. Yuan, Y. Ji, J. Jiang, Effect of corrosion layer of steel bar in concrete on time-variant corrosion rate, Mater Struct, 42 (2009) 1443-1450.
[67] T.D. Marcotte, C.M. Hansson, The influence of silica fume on the corrosion resistance of steel in high performance concrete exposed to simulated sea water, J Mater Sci, 38 (2003) 4765-4776.
[68] Y.-s. Ji, M. Wu, Z. Tan, F. Gao, F. Liu, Process control of reinforcement corrosion in concrete. Part 2: Time-dependent dominating factors under different environmental conditions, Constr Build Mater, 73 (2014) 214-221.
[69] M. Raupach, Investigations on the influence of oxygen on corrosion of steel in concrete - Part I, Mater Struct, 29 (1996) 174-184.

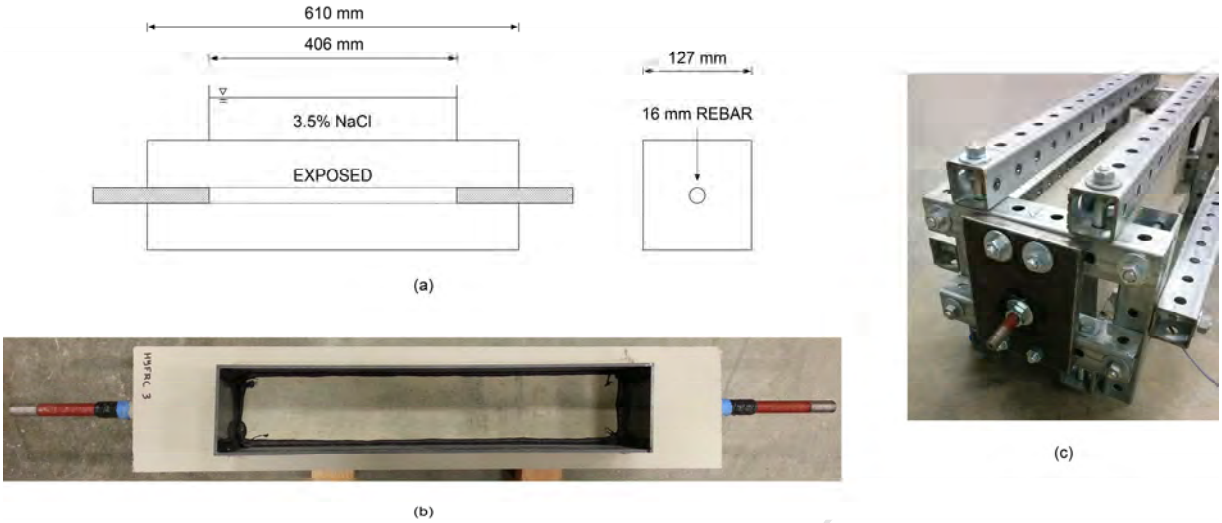

Figure 1: Details of specimen design: (a) Geometric drawing; (b) Plan view of specimen with ponding dam fixed to concrete surface; (c) Specimen in loading frame.

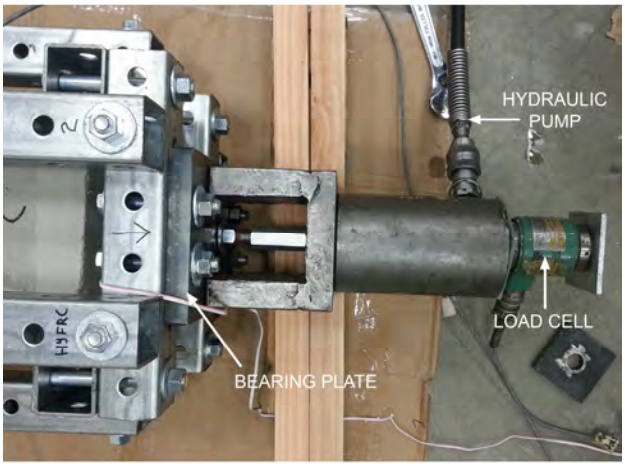

(a)

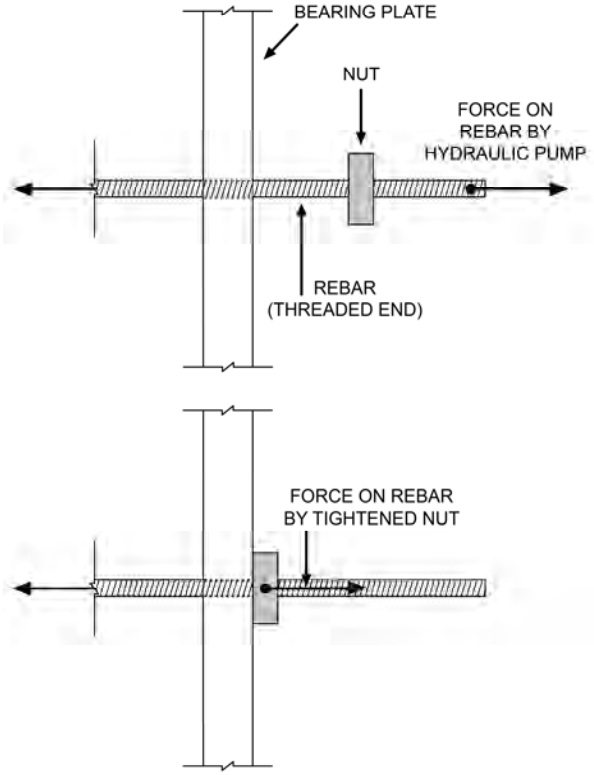

(b)

Figure 2: Specimen with loading frame: (a) During tensile loading, showing a hydraulic pump applying load onto the free end of the extruded reinforcing bar; (b) Loading schematic highlighting transfer of load on rebar from hydraulic pump to nut upon tightening of the nut.

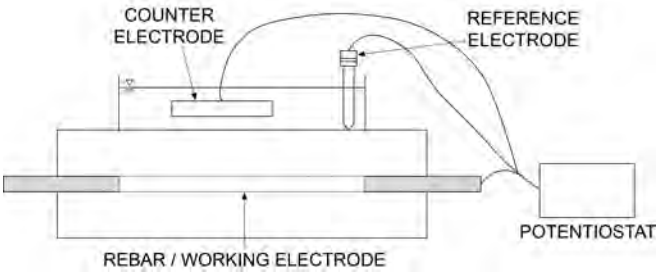

Figure 3: Electrochemical measurement setup using a three-electrode setup. Stainless steel is used as the counter electrode and a saturated calomel electrode (SCE) is used as the reference electrode.

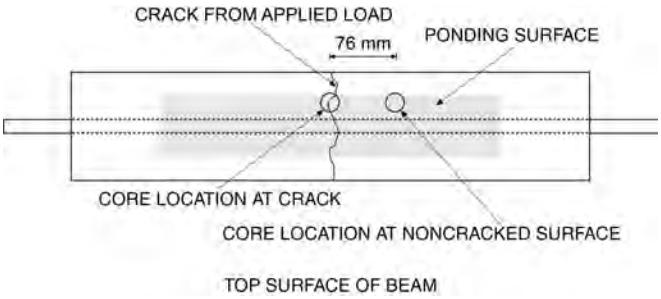

Figure 4: Schematic showing top, ponded surface of prism and coring locations of a loaded sample.

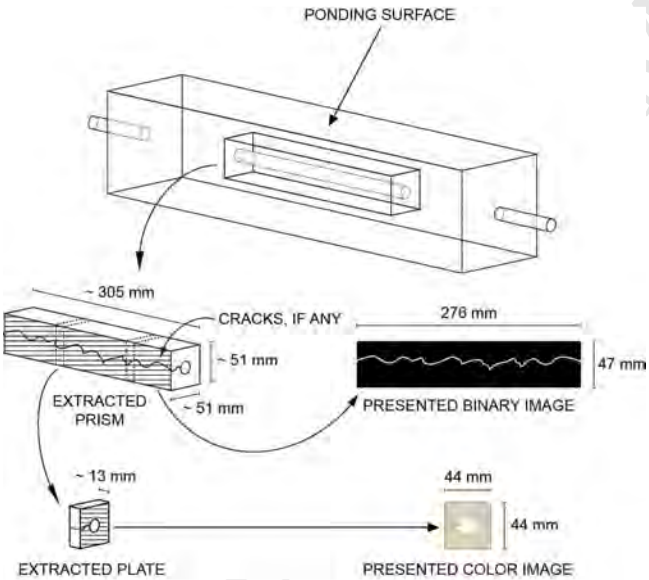

Figure 5: Schematic detailing extracted prisms and extracted plates used for optical imaging in Figure 7 and Figure 8. The hatched surfaces of the prism and plate indicate where imaging of the presented binary image and presented color image, respectively, occur.

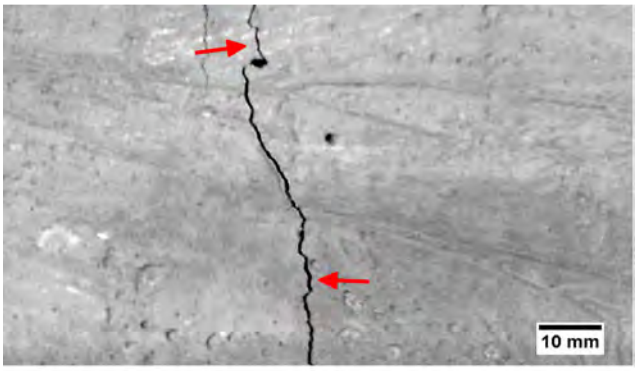

(a) C-L

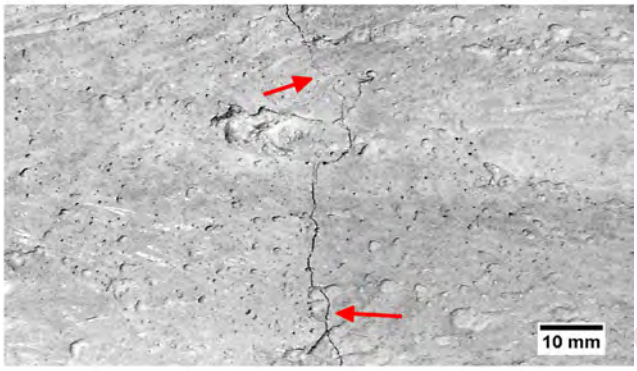

(b) HyFRC-L

Figure 6: Representative surface tensile cracking after applied loading and prior to environmental conditioning: (a) C-L; (b) HyFRC-L. Images are presented in grayscale to improve feature contrast.

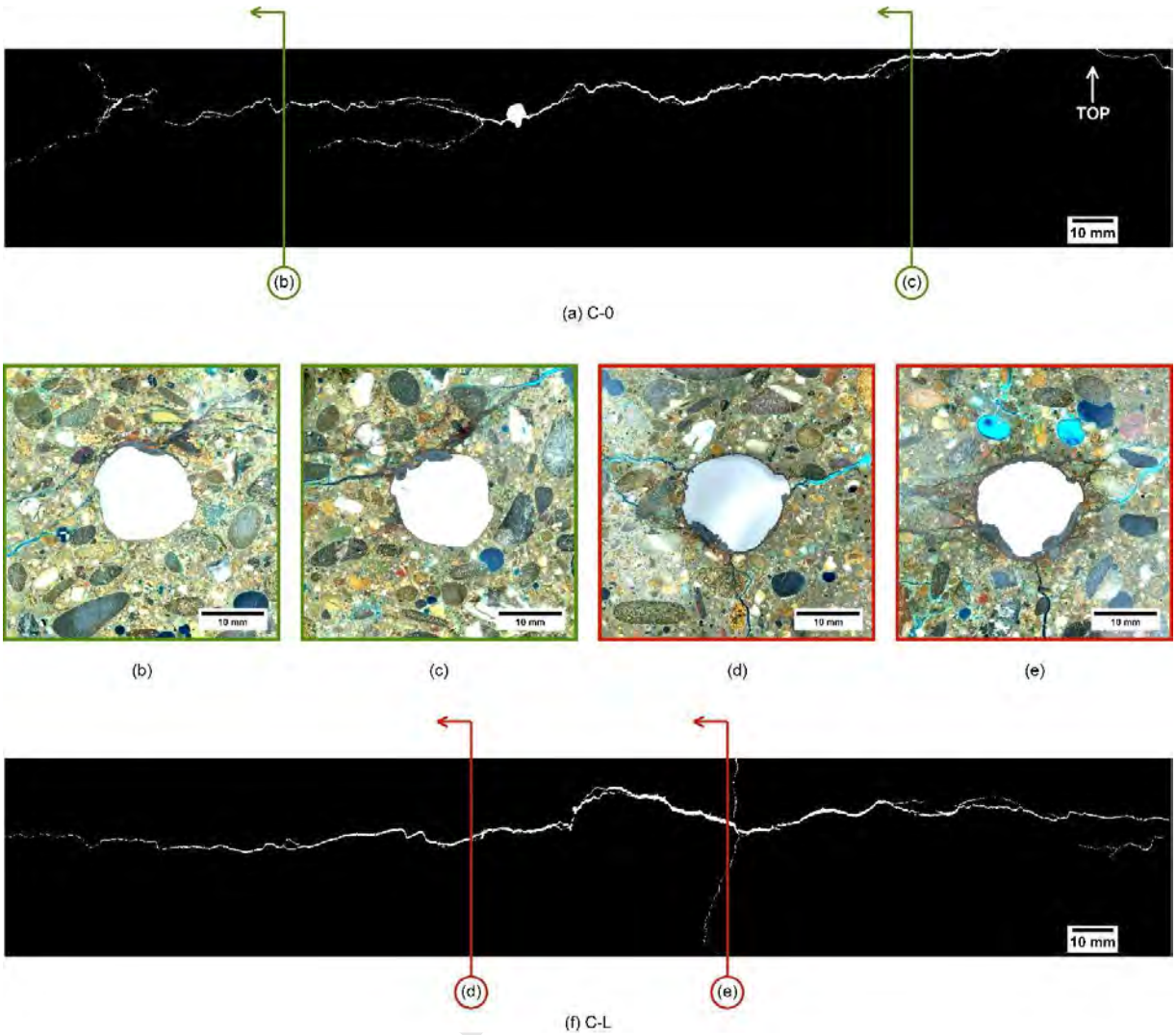

Figure 7: Sectional images of reinforced concrete specimens at the conclusion of environmental conditioning: (a)-(c) C-0; (d)-(f) C-L. Colored vertical lines on binary images indicate locations of indicated transverse section cuts. Binary images are used to highlight crack locations on a vertical surface of the extracted prism (as in Figure 5). A blue-colored epoxy was used to impregnate cracks and voids in transverse section views.

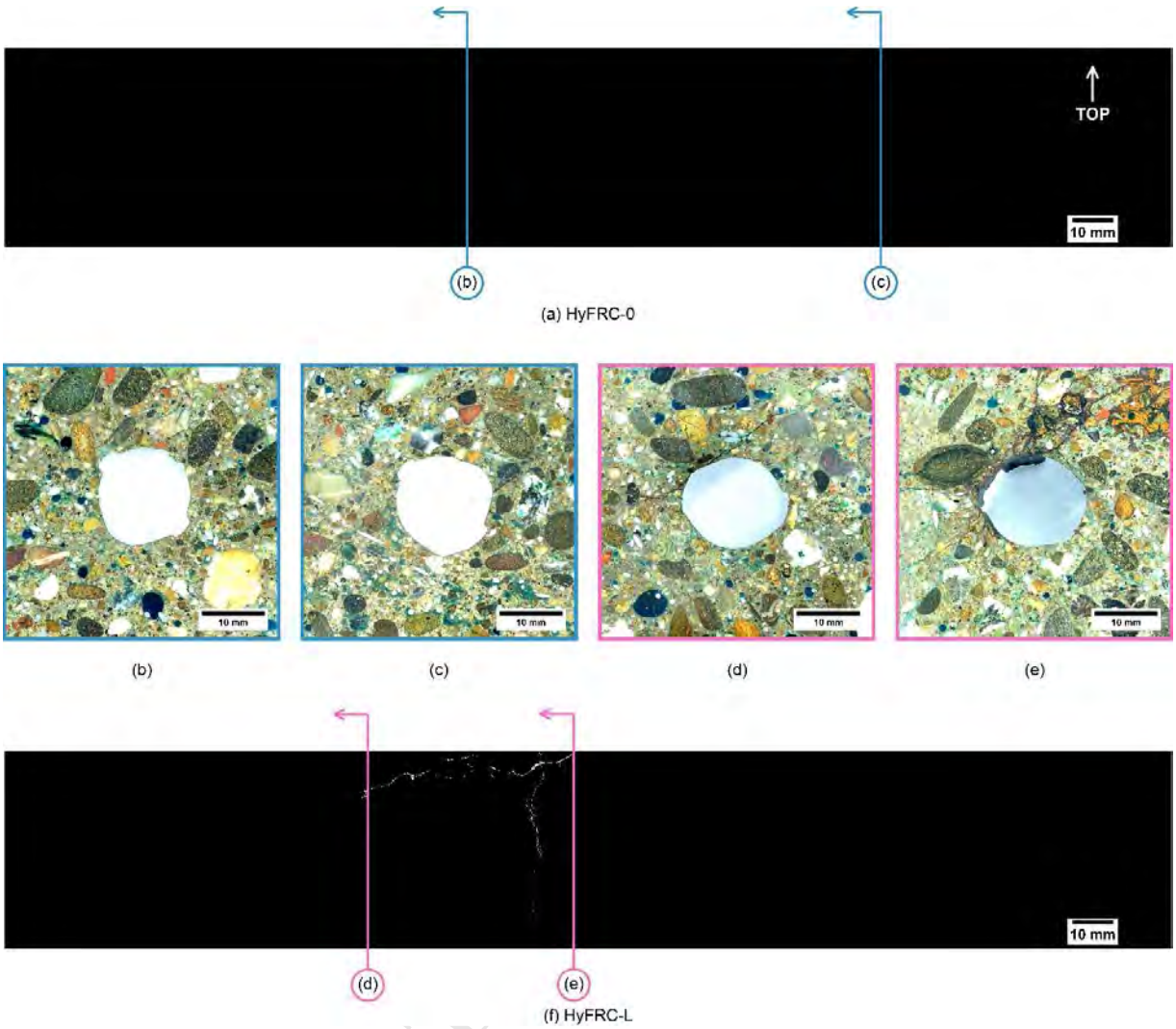

Figure 8: Sectional images of reinforced HyFRC specimens at the conclusion of environmental conditioning: (a)-(c) HyFRC-0; (d)-(f) HyFRC-L. Colored vertical lines on binary images indicate locations of indicated transverse section cuts. Binary images are used to highlight crack locations on a vertical surface of the extracted prism (as in Figure 5). A blue-colored epoxy was used to impregnate cracks and voids in transverse section views.

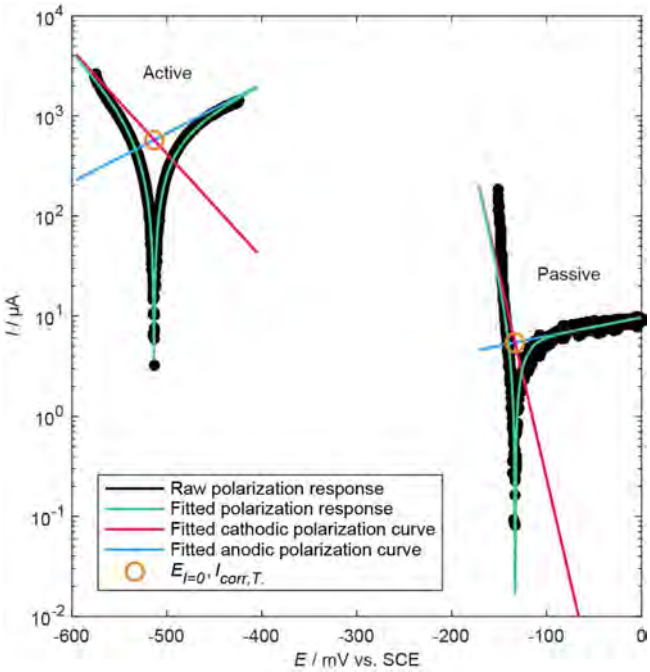

930
931 Figure 9: Typical fitting result of Tafel polarization curves for a passive sample and an active sample.

932

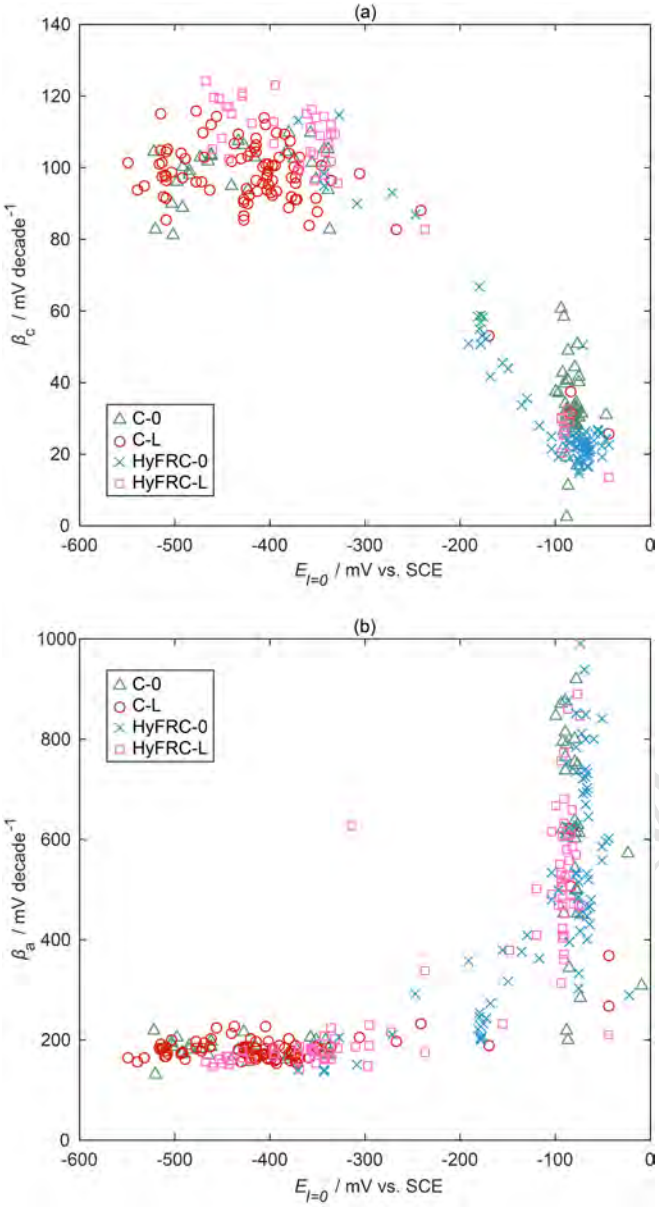

Figure 10: Tafel coefficients versus potential where no net current occurs $E_{I=0}$: (a) Cathodic Tafel coefficient β_c; (b) Anodic Tafel coefficient β_a.

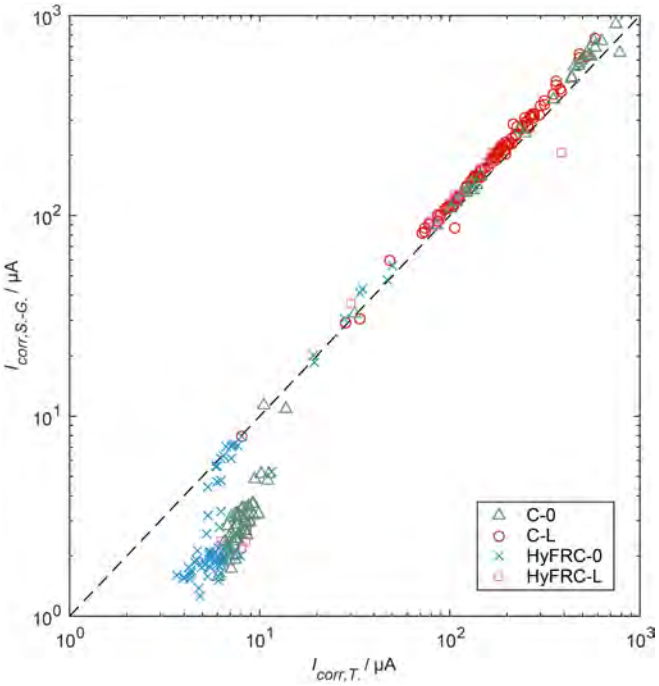

Figure 11: Correlation between corrosion current obtained between Stern-Geary equation $I_{corr,S.-G.}$ and Tafel polarization extrapolation $I_{corr,T.}$.

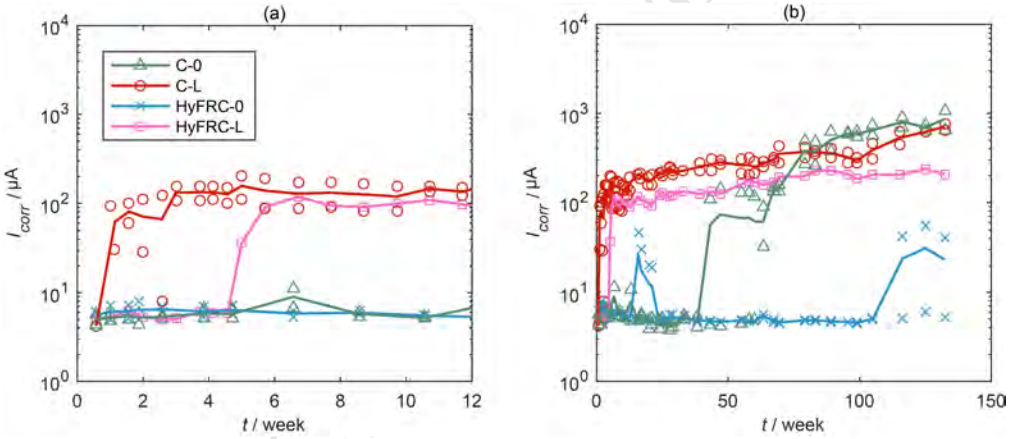

Figure 12: Corrosion current of samples: (a) During initial 12 weeks of environmental conditioning; (b) Complete experimental duration. Averaged responses of a specimen set are plotted as lines, while individual specimens are plotted as markers.

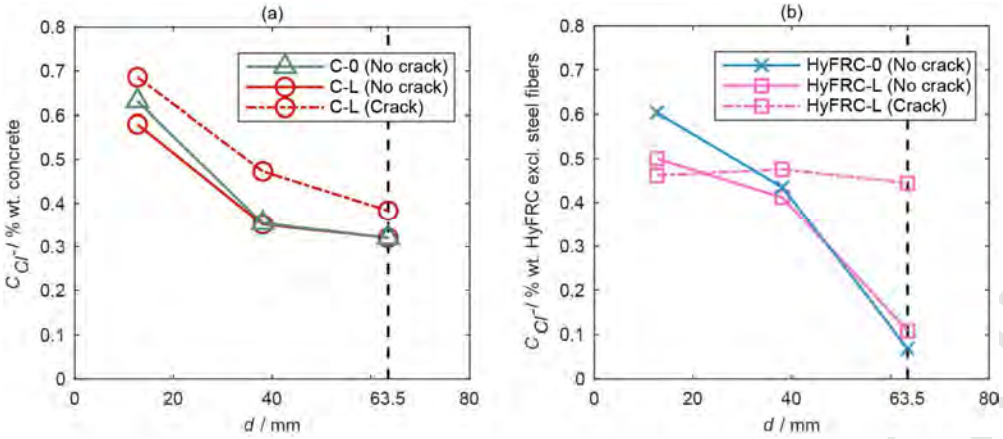

Figure 13: Chloride content profiles: (a) Concrete; (b) HyFRC. After specimen type designation, (Crack) refers to a core taken directly at an applied tensile load-induced crack location and (No crack) refers to a core taken at a location where no visible surface cracking at the ponding surface occurred. Dashed vertical line in plots indicates the depth at which the centroid of the steel reinforcing bar was located.

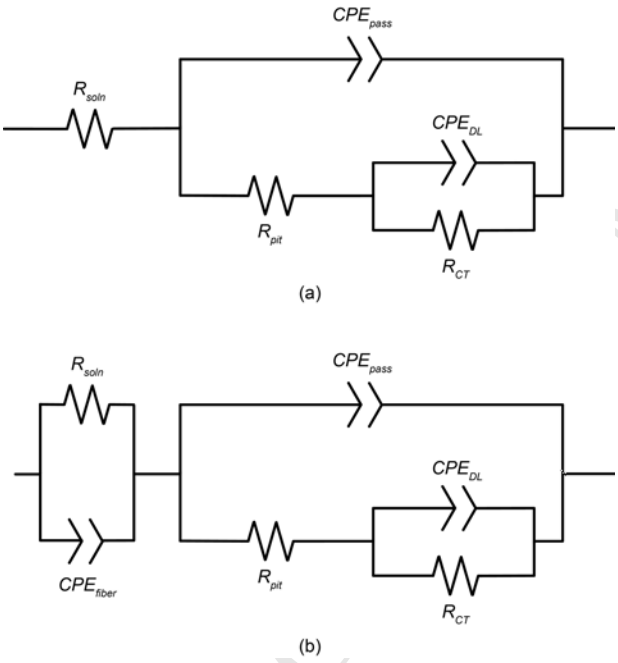

Figure 14: Equivalent electrical circuit model used for EIS results: (a) Reinforced concrete; (b) Reinforced HyFRC. CPE_{DL} represents the double-layer capacitance, CPE_{pass} represents the passive film interface, CPE_{fiber} represents the presence of steel fiber-matrix interfaces (in HyFRC composites only), R_{CT} represents the charge-transfer resistance, R_{pit} represents the resistance within pits, and R_{soln} represents the ohmic resistance in the matrix pores or cracks.

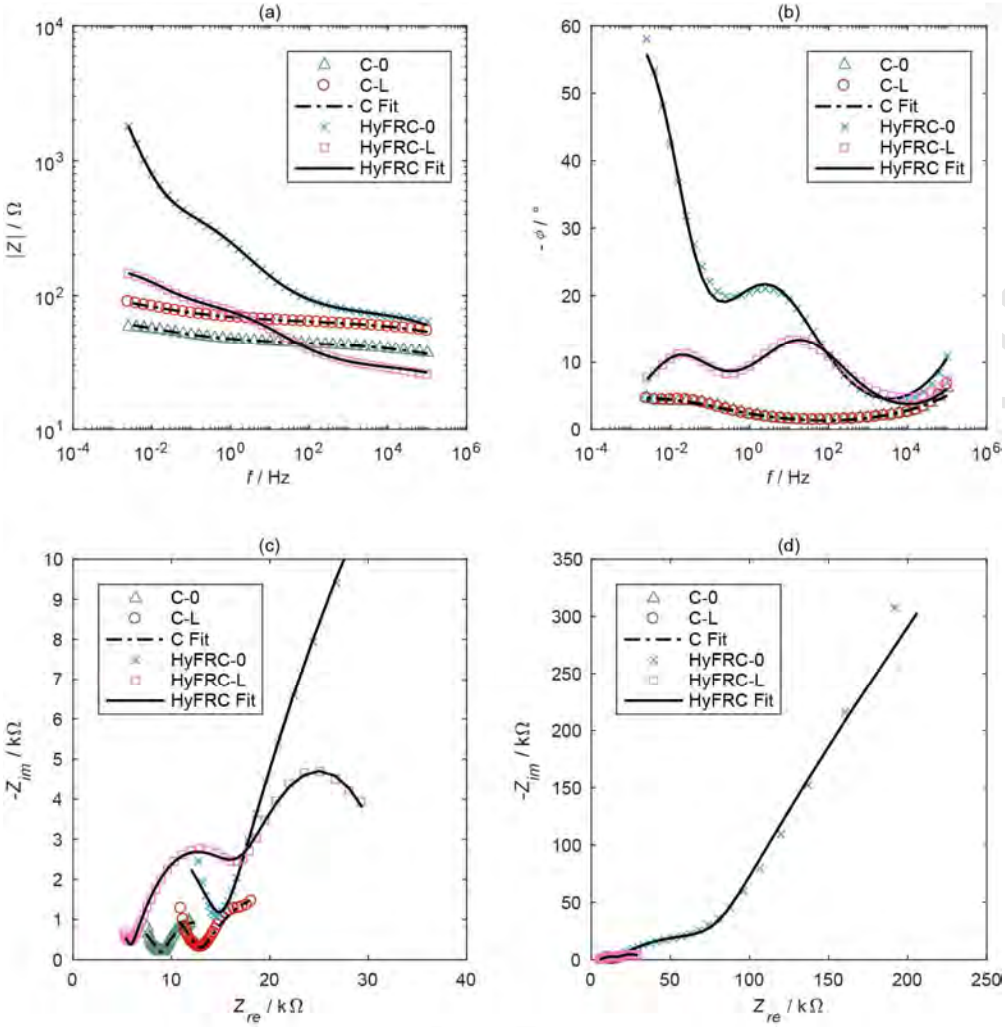

Figure 15: Plots showing EIS results and fitted results: (a) Bode plot with impedance modulus $|Z|$ versus frequency f; (b) Bode plot with negative phase shift $-\Phi$ versus frequency f; (c)-(d) Nyquist plots with the negative imaginary part $-Z_{im}$ of complex impedance versus the real part Z_{re} of the complex impedance. EIS measurements were performed at the conclusion of the environmental conditioning period.

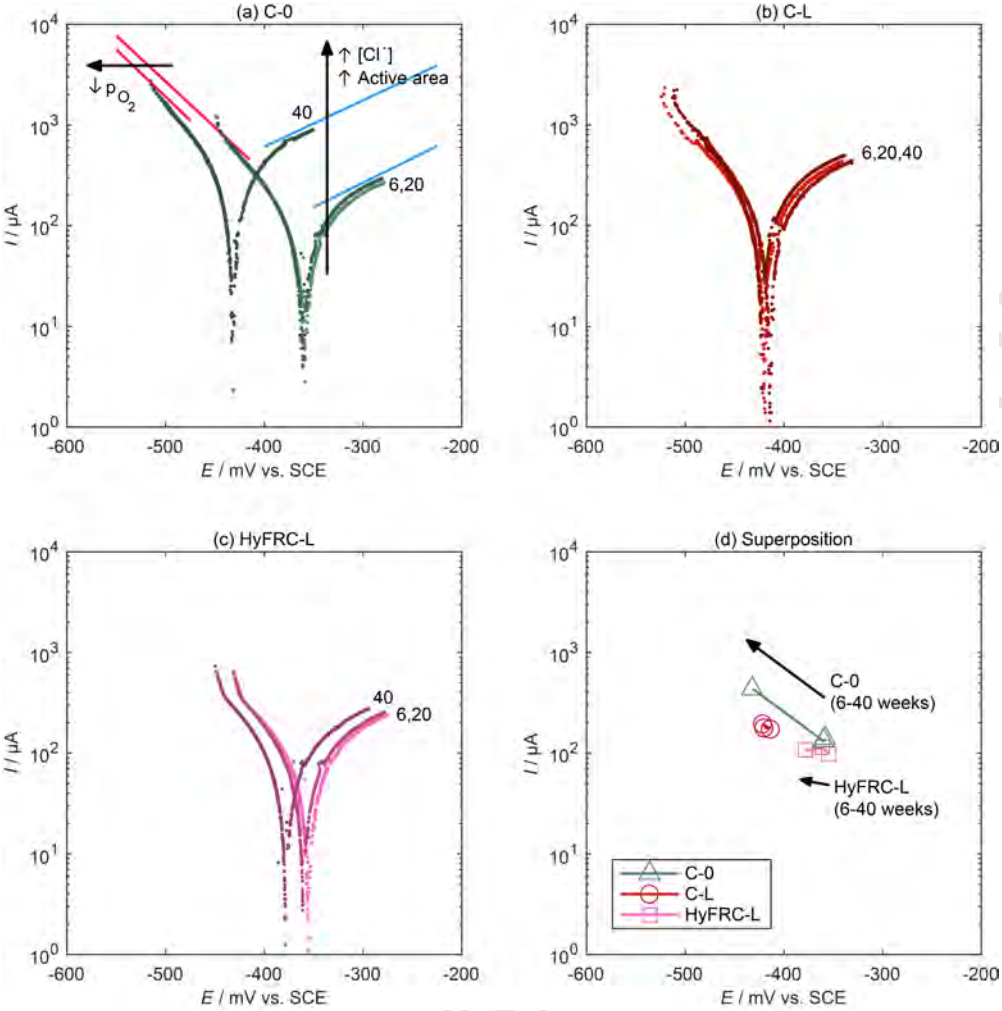

964
965 Figure 16: Tafel polarization responses of select specimens over elapsed active corrosion time, up to 40 weeks: (a)
966 C-0, additionally showing influence of factors on polarization curvature; (b) C-L; (c) HyFRC-L; (d) Superposition
967 of $I_{corr,T.}$-$E_{I=0}$ relations from (a)-(c). Numbers adjacent to polarization curves indicate time, in weeks, of elapsed
968 active corrosion.

969

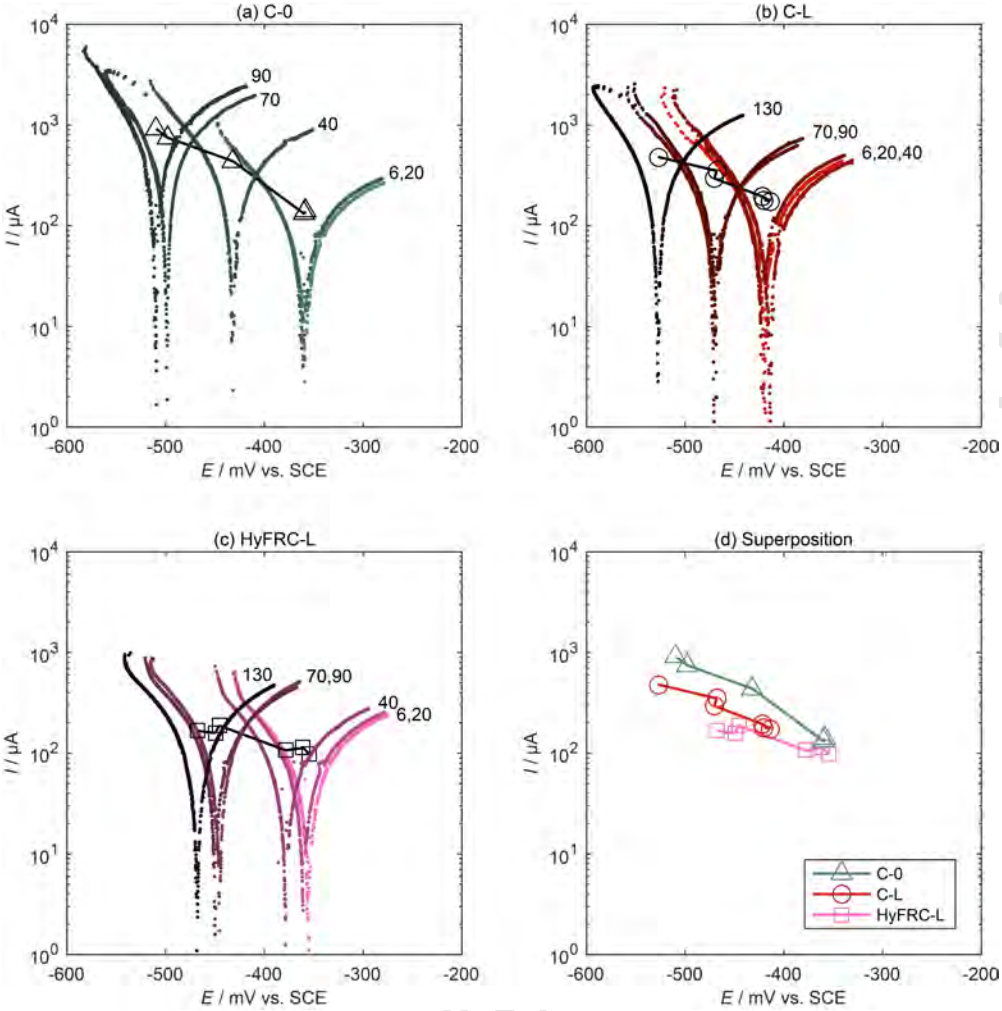

Figure 17: Tafel polarization responses of select specimens over elapsed active corrosion time, up to 90 or 130 weeks: (a) C-0; (b) C-L; (c) HyFRC-L; (d) Superposition of $I_{corr,T.}$-$E_{I=0}$ relations from (a)-(c). Numbers adjacent to polarization curves indicate time, in weeks, of elapsed active corrosion.

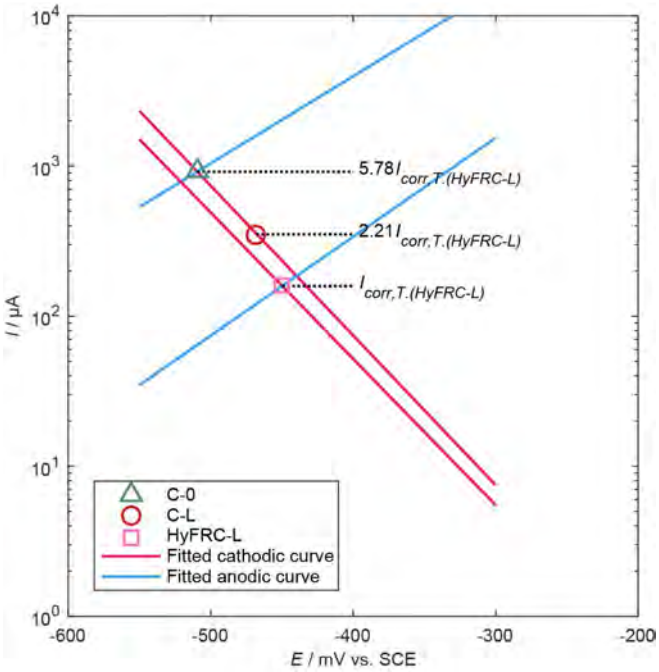

Figure 18: $I_{corr,T.}$-$E_{I=0}$ relations at 90 weeks, showing select fitted cathodic and anodic reaction curves from Tafel polarization responses. The corrosion current of HyFRC-L in the plot is referred to as $I_{corr,T.(HyFRC-L)}$.

979 Table 1: Survey of reinforced concrete polarization studies.

Reference	Binder type[1]	Total exposure duration	Concrete cracking in samples	Passive			Active		
				β_c (mV/dec.)	β_a (mV/dec.)	B (mV)	β_c (mV/dec.)	β_a (mV/dec.)	B (mV)
Babaee and Castel [25]	FA, ultra-fine FA, GGBFS, NaOH solution, Na_2SiO_3 solution	0.9 years[2]	No cracks found	30-45	Infinity	13-20	106-221	430-Infinity	43-69
Chang et al. [27]	C, FA	4.7 years	Not reported	-	-	-	192-263	450-800	63-86
	C, GGBFS			-	-	-	235-480	230-295	52-62
Alonso et al. [29]	OPC	6 years	Not reported	-	-	-	441 (Ambient) 289 (Damp)	10^{20}	-
Al-Tayyib and Khan [30]	C	2 years	Not reported	-	-	-	250-350	400-500	-
Subramaniam and Bi [26]	OPC	0.5 years	Crack induced by mechanical loading prior to chloride exposure	-	-	-	205	435	-
Glass and Chadwick [28]	OPC	2.5 years[2]	Not reported	-	-	-	160	-	-
	OPC, GGBFS								
Andrade and González [22]	OPC	30 days	Not reported	-	-	52	-	-	26
	Slag cement								
	Pozzolanic cement								
Grubb et al. [31]	OPC	0.4 years[2]	Microcracks found in plain mortar; No microcracks found in fiber-reinforced mortar	-	-	-	-	-	7-10 (Plain mortar)
									8-15 (Fiber-reinforced mortar)

980 [1] Binder type abbreviations: OPC - ordinary portland cement; FA - fly ash; GGBFS - ground granulated blast-
981 furnace slag; C - unspecified cement.

982 [2] Estimated duration in years.

983
984 Table 2: Batch proportions per cubic meter of concrete.

Composite	Portland cement (kg)	Aggregates (kg)		Water (kg)	Fibers (% vol. composite)		
		Coarse	Fine		PVA	Steel (30-mm length)	Steel (60-mm length)
Concrete	423	742	872	228	-	-	-
HyFRC	423	775	853	228	0.2	0.5	0.8

985
986
987
988
989
990
991
992
993 Table 3: Chemical composition of select reinforced concrete materials, expressed in mass percentage of material.

Material	CaO	SiO_2	MgO	Al_2O_3	Fe_2O_3	K_2O	Na_2O	TiO_2	P_2O_5	MnO			
Type I/II portland cement	61.08	20.36	4.14	3.66	3.09	0.53	0.22	0.22	0.08	0.06			
	C	Al	Si	P	S	Ti	V	Cr	Mn	Ni	Cu	Nb	Mo
A706 rebar steel	0.29	-	0.17	0.010	0.041	-	0.030	0.06	0.86	0.08	0.28	0.004	0.020
Fiber (30-mm length) steel	0.062	<0.005	0.07	0.011	0.006	<0.005	<0.005	0.05	0.30	0.05	0.08	-	<0.01
Fiber (60-mm length) steel	0.074	<0.005	0.13	0.015	0.007	<0.005	<0.005	0.05	0.32	0.05	0.09	-	<0.01

Table 4: Specimen type designation.

Composite	Nonloaded	Loaded
Reinforced concrete	C-0	C-L
Reinforced HyFRC	HyFRC-0	HyFRC-L

Table 5: Summary of Tafel coefficients and Stern-Geary coefficient.

	Passive			Active		
	β_c (mV/dec)	β_a (mV/dec)	B (mV)	β_c (mV/dec)	β_a (mV/dec)	B (mV)
Mean value (standard deviation)	19.8 (4.26)	562 (201)	8.31 (1.81) 24.0[a]	102 (9.74)	180 (40.4)	28.1 (2.83)

[a] Empirical mean value based on fitting of corrosion current values from Stern-Geary equation to extrapolated corrosion current values from Tafel polarization.

Table 6: Element values for equivalent electrical circuit.

	I_{corr}	R_{soln}	R_{CT}	CPE_{DL}-Y_0	CPE_{DL}-α	R_{pit}	CPE_{pass}-Y_0	CPE_{pass}-α	CPE_{fiber}-Y_0	CPE_{fiber}-α
	μA	Ω	Ω	mS s^{α}	-	Ω	mS s^{α}	-	mS s^{α}	-
C-0	1070	3.07	33.6	119	0.336	41.0	0.103	0.306	-	-
C-L	775	6.93	63.3	81.3	0.297	56.7	0.056	0.325	-	-
HyFRC-0	5.26	74.1	3.07 x 10^5	12.2	0.807	431	1.42	0.512	5.86 x 10^{-3}	0.493
HyFRC-L	208	28.8	77.7	73.3	0.632	61.5	2.58	0.502	5.67 x 10^{-3}	0.508

Highlights:

1. Corrosion products form matrix cracks that are resisted by fiber reinforcement.
2. Corrosion-induced cracks result in greater anodic current response.
3. Stern-Geary coefficient for active corrosion determined to be B=28.1 mV.
4. Lower ohmic matrix and charge transfer resistances for greater cover cracking and rebar pitting.
5. Lower exponent α of CPE in EIS equivalent circuit for greater steel pitting.